

MReadings: MR in RT

9th Edition, ASTRO 2023

[siemens-healthineers.com/magnetom-world-rt](https://www.siemens-healthineers.com/magnetom-world-rt)

Page 02

Editorial Comment

Yue Cao

Page 04

Dose Calculation on Synthetic CT and Related Patient-Specific Quality Assurance for MR-Only Radiotherapy Planning for the Male Pelvic Region

Riccardo Dal Bello, et al.

Page 16

Evaluation of the Contour 24 Coil for an MR-Only Radiotherapy Workflow

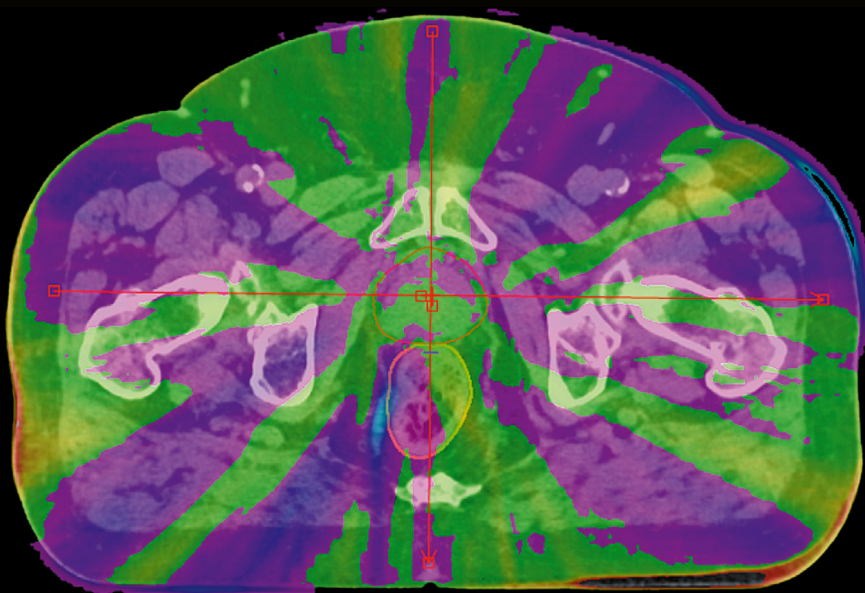
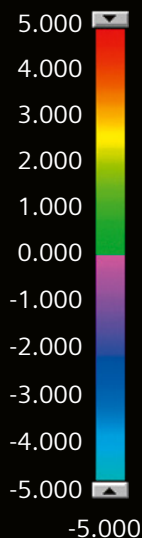
Marimuthu Sankaralingam, et al.

Page 31

Bring-Your-Own-Phantom: A Flexible Stand-Alone Distortion Analysis Prototype

Niranjan Venugopal, et al.

Dose Color Wash [Gy]
5.000



Point-wise absolute dose-difference map



Yue Cao, Ph.D., FAAPM, professor of Departments of Radiation Oncology, Radiology, and Biomedical Engineering, University of Michigan, has led a functional imaging laboratory for development of MRI acquisition and reconstruction techniques, image processing and physiological information quantification primarily related to radiation therapy (RT) applications and utilities for 20 years.

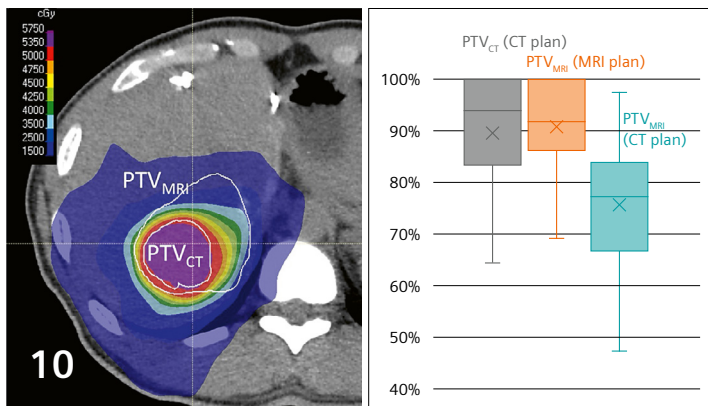
Dear readers and colleagues,

Since its introduction as a diagnostic tool in the 1980s, MRI has been used to support radiation target definition for intracranial tumors. Thanks to world-wide availability and numerous technological advancements, MRI is now used routinely for delineation of gross tumor volumes and organs-at-risk for RT treatment planning for a large variety of indications including primary and metastatic brain tumors, hepatocellular carcinoma, rectal cancer, prostate cancer, breast cancer and nasopharynx cancer. 4D-MRI supports management of respiratory motion for abdominal tumor treatments. Multiparametric MRI has been explored for definition of tumor sub-volumes to be targeted for focal radiation boosting as well as for mapping the heterogeneous function of organs-at-risk to guide individualized treatment strategies for better tumor local control and reduction of normal tissue toxicity.

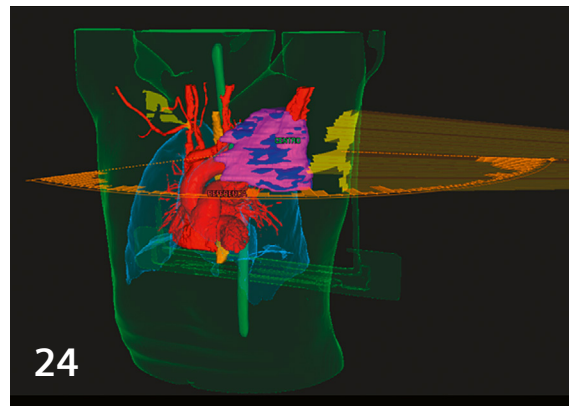
To help support robust and efficient utilization of MRI in RT, the seven articles in this volume discuss techniques, experiences and barriers in MR-only workflows, geometric distortion management, dose calculation based on MRI-synthesized CT, and quality assurance as well as MRI-based motion management strategies for treatment planning of liver and breast cancers.

A handwritten signature in cursive script that reads "yue cao".

Yue Cao



4D-MRI for Treatment Planning of Liver Tumors



The Effect of Radiation Therapy on Vessels and Circulating Blood

Editorial Comment

2 Editorial Comment

Yue Cao

Departments of Radiation Oncology, Radiology and Biomedical Engineering, University of Michigan, Ann Arbor, MI, USA

20 A Breast MR-in-RT Workflow: Motion Assessment of Breast and OAR with 4D Self-Gating MRI

Sylvain Doussin, et al.

Siemens Healthineers, Erlangen, Germany

24 The Forgotten Effect of Radiation Therapy on Vessels and Circulating Blood

Felipe A. Calvo, et al.

Department of Radiation Oncology, Clínica Universidad de Navarra, Madrid, Spain

Radiation Therapy

4 Dose Calculation on Synthetic CT and Related Patient-Specific Quality Assurance for MR-Only Radiotherapy Planning for the Male Pelvic Region

Riccardo Dal Bello, et al.

Department of Radiation Oncology, University Hospital Zurich and University of Zurich, Switzerland

10 4D-MRI for Treatment Planning of Liver Tumors

Jessica Scholey, et al.

Department of Radiation Oncology, University of California, San Francisco, CA, USA

16 Evaluation of the Contour 24 Coil for an MR-Only Radiotherapy Workflow

Marimuthu Sankaralingam, et al.

Radiotherapy Physics, Beatson West of Scotland Cancer Centre, DCPB, NHS GGC, Glasgow, UK

31 Bring-Your-Own-Phantom (BYOP): A Flexible Stand-Alone Distortion Analysis Prototype

Niranjan Venugopal, et al.

Department of Medical Physics, CancerCare Manitoba, Winnipeg, MB, Canada;

Department of Physics and Astronomy; Department of Radiology, University of Manitoba, Winnipeg, MB, Canada

Meet Siemens Healthineers

38 Introducing Patrick Kupelian

VP of Medical Affairs at Varian, a Siemens Healthineers Company, and Professor of Radiation Oncology at UCLA, Los Angeles, CA, USA

Dose Calculation on Synthetic CT and Related Patient-Specific Quality Assurance for MR-Only Radiotherapy Planning for the Male Pelvic Region

Riccardo Dal Bello¹, Francesca Nella¹, Bertrand Pouymayou¹, Michael Christian Mayinger¹, Andreas Hötter², Matthias Guckenberger¹, Stephanie Tanadini-Lang¹

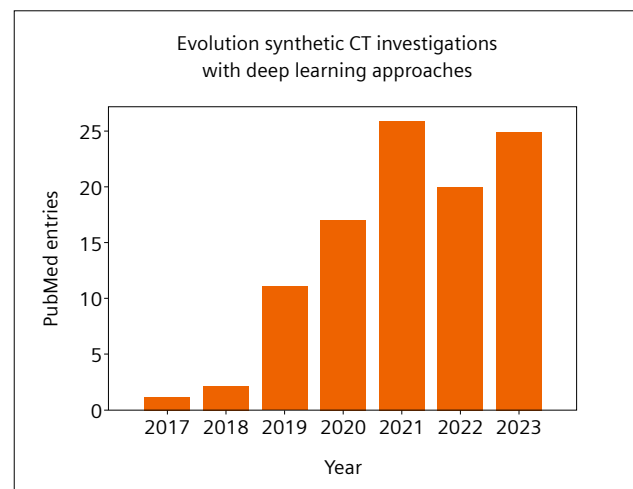
¹Department of Radiation Oncology, University Hospital Zurich and University of Zurich, Switzerland

²Department of Diagnostic and Interventional Radiology, University Hospital Zurich and University of Zurich, Switzerland

Introduction

Radiation therapy (RT) planning is classically based on computed tomography (CT). This derives from the fact that the CT voxel values, i.e., Hounsfield units (HU), have a monotonic correlation with the electron density, which in turn is required for the dose calculations in RT plans [1]. Improved results may be achieved with dual-energy CT (DECT) [2]. Nonetheless, while CT and DECT imaging are the preferable methods for performing dose calculations, additional imaging modalities have been introduced to the RT workflow during the past decades to improve the identification and contouring of target volumes and organs at risk (OAR). The use of positron emission tomography (PET) and magnetic resonance (MR) imaging as additional modalities is nowadays the standard of care for multiple treatment sites [3, 4]. In particular, the use of MR for RT is currently rapidly expanding, partly driven by the clinical introduction of hybrid MR-linac systems [5, 6]. Target and OAR contouring is therefore preferably performed on the MR data, exploiting the superior soft-tissue contrast and functional information acquired using dedicated sequences. The use of the CT data during treatment planning is then limited to dose calculation. In order to simplify the workflow and reduce the patient's radiation exposure, replacing the planning CT examination with "synthetic CT" (sCT) derived from the MR data has been proposed [7]. This would pave the way for MR-only RT planning. The seminal work by Han in 2017 has demonstrated the superiority of deep learning (DL) approaches for converting MR to sCT [8]. Figure 1 shows the rapid and steady expansion of this research field. Several commercial solutions are now available, and the value of sCT for dose calculation and

matching to cone beam CT (CBCT) or kV imaging on image-guided RT (IGRT) linacs for patient positioning has been reported [9–12]. Novel challenges and dedicated solutions have been described for performing MR simulations in the RT position, including immobilization equipment [13]. Quality assurance guidelines are available for MR scanners used in RT applications [14], but only limited experience is available in the literature for patient-specific quality assurance of sCT data generated with DL approaches [15]. In this report, we focus on the clinical commissioning of the dose calculation and the implementation of patient-specific quality assurance for this task.



1 Evolution of the research field¹ of deep learning-generated synthetic computed tomography for radiotherapy planning.

¹Search query: ("synthetic ct" or "sct" or "pseudo ct" or "synthetic computed tomography" or "pseudo computed tomography") and ("radiotherapy" and "dose") and ("deep learning" or "neural network" or "artificial intelligence")

Clinical workflow for RT planning

Imaging data acquisition

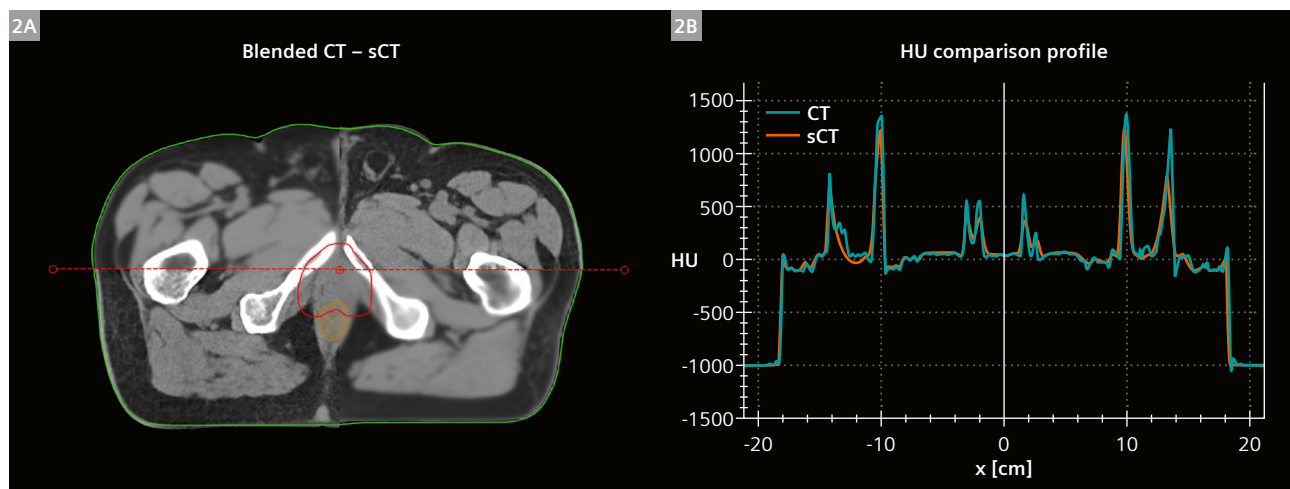
CT and MR data acquisition is the first task to be completed for the treatment-planning workflow. If eligible for MR examinations, male patients referred for pelvic RT at the Radiation Oncology Department of University Hospital Zurich are examined for both modalities in the RT treatment position. This setup includes a flat table top, flex body coils fixed on arcs to avoid compressing the abdomen and deforming the patient contour, and knee and feet rests to achieve reproducible patient positioning. MR simulations are performed on a 1.5T MAGNETOM Sola scanner (Siemens Healthcare, Erlangen, Germany), and CT simulations are performed on a SOMATOM Definition AS scanner (Siemens Healthcare, Forchheim, Germany). The MR examination includes sequences dedicated to diagnostics and contouring, adjusted to our institutional requirements (T1 StarVIBE, T2 turbo spin echo, diffusion-weighted imaging). Siemens Healthineers provided sequences for sCT generation (T1 VIBE/Dixon). The total examination time ranges from 30 to 45 minutes. The latter is acquired with a native resolution of 1.6 mm in-plane and 2 mm slice thickness with transversal orientation. The coverage is up to half of the L1 vertebral body and includes couch markers positioned posterior to the patient. All sequences are acquired with activated 3D distortion correction and cardinal slice directions (transversal, sagittal, or coronal) without any tilt angles. The data is then sent to the hospital's PACS and the department's treatment planning system (TPS) for diagnostic reporting and RT treatment planning, respectively.

Synthetic CT generation

The MR Dixon scans are reconstructed directly at the scanner to produce four 3D images: in-phase, opposed-phase, water, and fat. The first two reconstructions are provided as input data for *syngo.via* RT Image Suite VB60 (Siemens Healthineers, Erlangen, Germany) to generate an sCT with continuous HU values matching the anatomy of the MR Dixon. Acquiring the dedicated sequence requires up to 5 minutes, which is similar for the sCT reconstruction, which sums up to a total time burden of up to 10 minutes. The process is performed while the patient is still inside the bore for the acquisition of additional diagnostic sequences. Therefore, if artifacts (e.g., due to erroneous FOV positioning) or uncommon anatomies (e.g., excessive rectal filling) are observed in the Dixon and sCT, these can be repeated at the end of the examination without requiring an additional appointment for the patient. A prompt inspection of the sCT reconstruction can be performed directly at the scanner using *syngo.via* RT Image Suite. Figure 2 shows a comparison with the planning CT performed in the Aria Eclipse V16.1 TPS (Varian, a Siemens Healthineers Company, Palo Alto, CA, USA).

Data post-processing for the TPS

The reconstructed MR and sCT data are transferred to MIM (MIM Software Inc, Cleveland, OH, USA) for post-processing, and then to the Aria Eclipse TPS for treatment planning. All data transfers are automated and performed via DICOM node. Aria stores the incoming DICOM data as



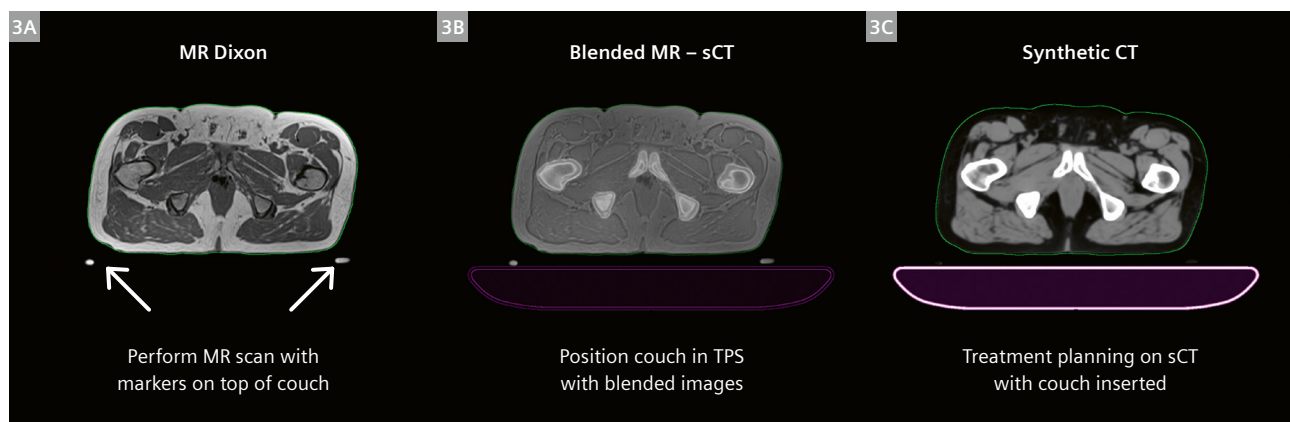
2 Comparison of sCT and planning CT data with checkerboard blending of the two images (2A). The PTV contour is reported in red. The line profiles with corresponding HU values in the left-to-right patient direction through the PTV are shown (2B).

2D slices, and the generation of the 3D volumes for selected sequences is automated by assigning an RTStruct in MIM before the last DICOM node transfer. Further post-processing, such as renaming the 3D volumes according to institutional guidelines, is automated using ESAPI scripts developed in-house. The sCT is resampled to a resolution of $1 \times 1 \times 1 \text{ mm}^3$ in order to provide adequate and standardized resolution for support structures and contours in the TPS. The support structures include the IGRT linac couch top, which should be included at the correct location to calculate the shifts used during the daily positioning, to evaluate the clearance of the linac gantry rotation, and to compute the dose considering the couch attenuation. The procedure for correctly placing the support structure is shown in Figure 3. Finally, contouring is performed in the dedicated Aria application. The MR sequences and the sCT share the same frame of reference UID and are therefore intrinsically registered. Since there may be a time

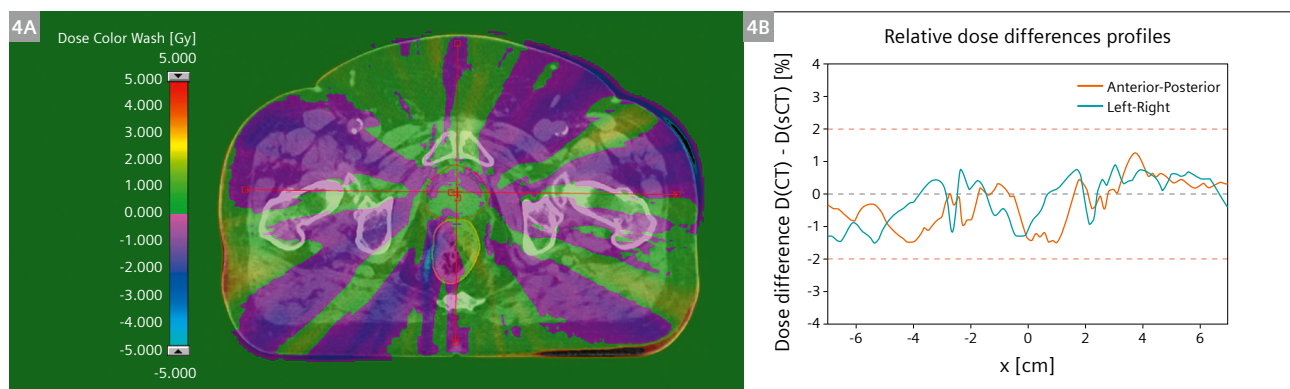
difference of up to 45 minutes between the first Dixon acquisition and the last diagnostic MR sequence, physiological changes (e.g., bladder filling) or patient movement (e.g., relaxation of the dorsal and gluteal muscles) might occur. In such cases, the MR dataset is extracted from the frame of reference, registered to the Dixon and sCT by an experienced radiation oncologist, and then used for contouring. The structure set is always assigned to the sCT.

Dosimetric commissioning

Volumetric modulated arc therapy (VMAT) treatment plans are prepared in the Aria Eclipse V16.1 TPS (N = 10 patients in this study). The settings used are beam quality 6X, two full arcs with opposed gantry rotation and different collimator angles, activated jaw tracking, and dose-to-medium calculation with Acuros V16.1 using a 1.5 mm grid resolution and normalization on the PTV Dmean. The plans are



- 3** Procedure for support-structure positioning in the TPS. **(3A)** MR markers are placed on top of the flat couch during the MR simulation. **(3B)** The markers are visible in the blended MR-sCT view and can be used for the IGRT couch positioning. **(3C)** Treatment planning on the sCT can proceed with the IGRT couch correctly placed.

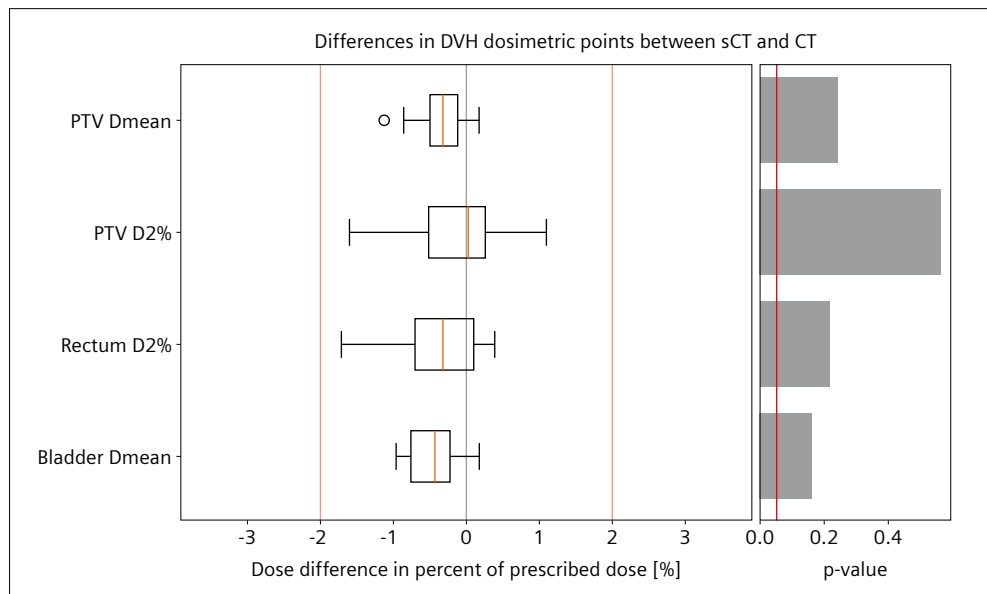


- 4** The point-wise absolute dose-difference map between the calculation on the CT and the sCT is shown for an example patient with prescription $5 \times 7.25 \text{ Gy}$ **(4A)**. Line profiles with the relative dose differences in the anterior-posterior and left-right direction crossing the PTV center are also reported **(4B)**. Reference horizontal lines at 0% and $\pm 2\%$ relative deviations are reported in grey and red, respectively.

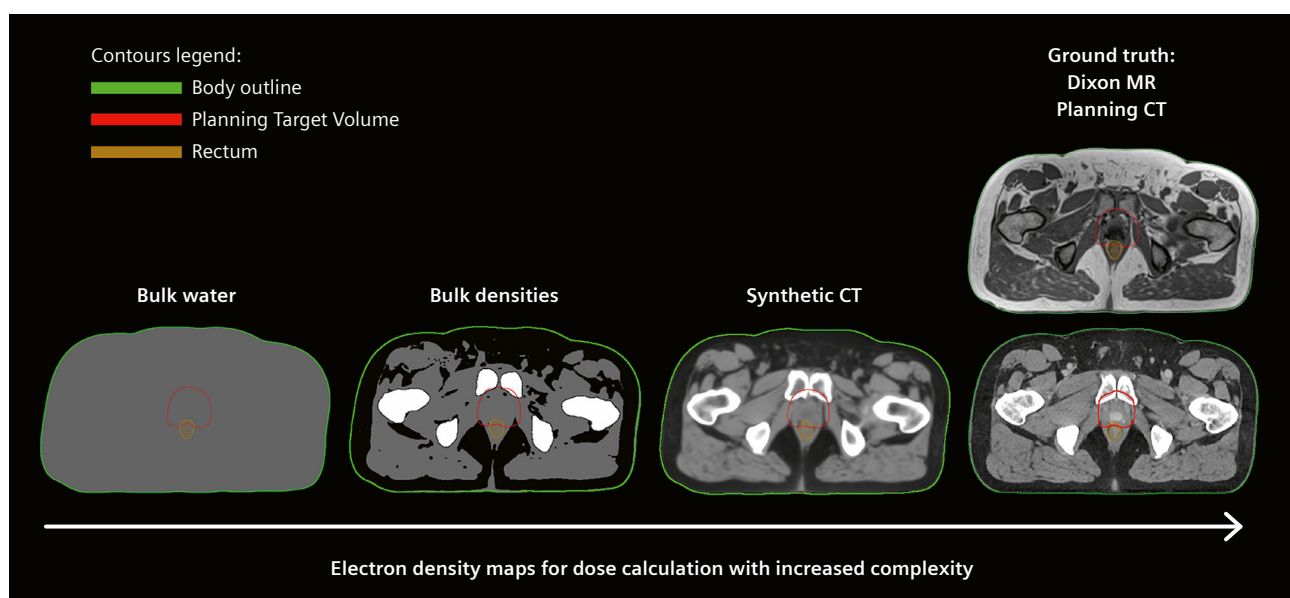
optimized on the sCT and rigidly copied and recalculated with a preset number of monitor units (MU) on the CT. Figure 4 shows a qualitative evaluation of the dose differences between the two calculations for an example patient. The quantitative analysis of multiple dose volume histogram (DVH) points is reported in Figure 5. The statistical analysis is performed with a Z-test (variance 1%, significance level $p = 0.05$, testing H_0 : dose difference is 0%) in line with previous literature [16].

Patient-specific quality assurance

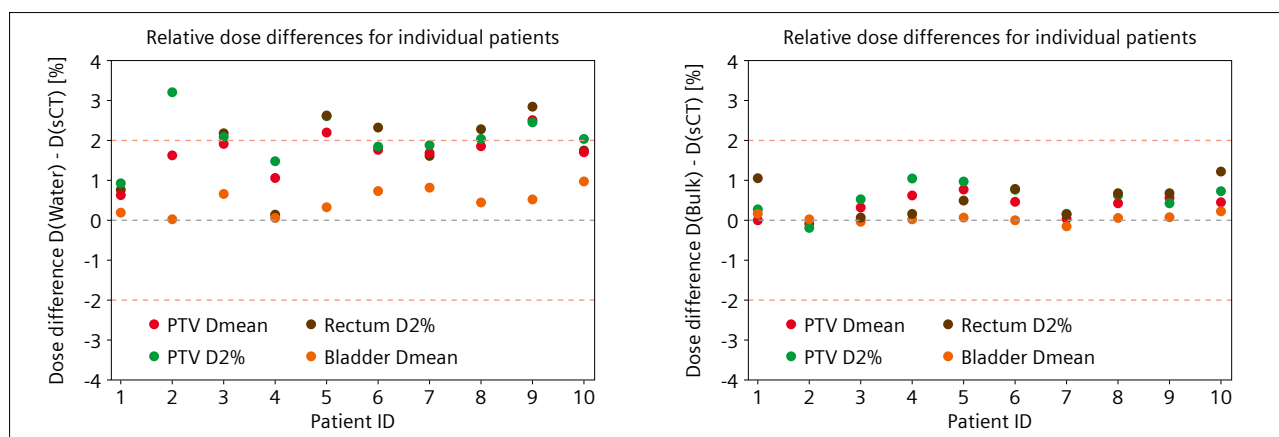
National and international recommendations for patient-specific quality assurance (PSQA) of intensity-modulated RT plans prescribe the use of independent secondary calculation software to verify the correctness of the MU to be delivered [17]. We use a similar approach for PSQA of the electron density map on which the dose is calculated, which in turn affects the number of MU predicted by the



5 Quantitative analysis of four DVH dosimetric points. The differences between dose calculation on sCT and CT are summarized with box plots (left). Reference vertical lines at 0% and $\pm 2\%$ relative deviations are reported in grey and red, respectively. The statistical Z-test shows that all parameters are non-significantly ($p = 0.05$) different from zero (right).



6 Patient-specific quality assurance approach with independent electron density maps of increasing complexity.



7 Dose differences for individual patients and selected DVH dosimetric points between the investigated PSQA methods (water (i) left; bulk densities (ii) right) and the reference calculation on the sCT. Reference horizontal lines at 0% and $\pm 2\%$ relative deviations are reported in grey and red, respectively.

DVH point	PTV Dmean	PTV D2%	Rectum D2%	Bladder Dmean
Relative deviations Water–sCT (Mean \pm Stdev)	$1.7 \pm 0.51\%$	$2.06 \pm 0.6\%$	$1.65 \pm 0.98\%$	$0.45 \pm 0.31\%$
Relative deviations Bulk densities–sCT (Mean \pm Stdev)	$0.34 \pm 0.27\%$	$0.51 \pm 0.37\%$	$0.51 \pm 0.41\%$	$0.02 \pm 0.1\%$

Table 1: Summary of the dose deviations observed between the investigated PSQA methods and the reference calculation on the sCT.

primary and secondary dose-calculation algorithms. The process is shown for an example case in Figure 6. The ground truth data is the Dixon MR and, when available, the planning CT. Four different models are evaluated to generate independent electron density maps: (i) bulk override of the patient body² with water, (ii) bulk overrides of four tissue classes³ based on contours generated on the Dixon MR, (iii) synthetic CT, and (iv) the planning CT. The electron density maps (i) and (ii) are generated with a dedicated ESAPI script in Aria Eclipse V16.1. The electron density map (iii) is generated in *syngo.via* RT Image Suite VB60. The planning CT (iv) is not considered in the following, assuming that it is not available for PSQA in an MR-only RT context. For the $N = 10$ patients included in the study, the differences in dose calculation between (i) and (ii) and the synthetic CT (iii) are reported in Figure 7 and Table 1. The method (i) shows outliers above 2%, but none above 4%, and systematic positive dose deviations. The method (ii) does not lead to any outlier above 2%, and the average dose deviations are within 1%.

²Body contour defined on the Dixon MR.

³HU(Air) = -1000, HU(Bone) = +400, HU(Fat) = -75, HU(Soft tissue) = +7.

Discussion

The transition toward MR-only RT relies on the availability of high-quality sCT, which should replace the need for a planning CT examination. This study reports on the results of dose calculations obtained using MR data acquired on a 1.5T MAGNETOM Sola scanner and then used to generate sCT with continuous HU on the *syngo.via* RT Image Suite VB60 software. The qualitative evaluation of the HU reconstruction (Fig. 2) and dose maps (Fig. 4) show the high level of equivalence between sCT and CT. The quantitative analysis (Fig. 5) shows non-significant dose differences between calculations performed on sCT and CT. These results support the use of sCT for treatment planning and dose calculation in the context of MR-only RT, without the need for a planning CT examination. This study also evaluates the PSQA methods to be used to verify the quality of the dose calculation on sCT if the planning CT data is not available, i.e., after the go-live phase in the clinical MR-only RT implementation. The use of an easily implementable but naïve recalculation of the treatment plans on bulk water may be valuable for identifying potential outliers with large errors in the HU reconstruction of the sCT, which lead to dose deviations above 5%. A more resource-

intensive approach requiring the contouring of four tissue classes on the Dixon MR is a robust method for potentially identifying smaller reconstruction errors leading to dose differences within a 2% threshold. These results should be compared to typical limits for PSQA recommendations that require MU equivalence between the primary and secondary dose calculation engines to the 3% level [17]. Moreover, generating data with DL approaches leads to an sCT that is based on large amounts of data in the software's training phase, is realistic, and can be inspected with dedicated applications. However, it does not allow direct human interpretation of the underlying conversion processes of MR to sCT. On the other hand, in the case of dose differences during the PSQA process, adopting a method based on bulk densities allows human interpretability. This approach provides the simultaneous use of a data-driven method (sCT) for the RT plan, and a preparation- and knowledge-driven one (bulk densities) for PSQA [18], which we combine to achieve a robust clinical implementation. Furthermore, a comprehensive PSQA procedure should encompass the validation of data-transfer integrity between the MR scanner, TPS, and DL for sCT generation. This study does not address these particular aspects. The primary focus of the current investigation is the dose-calculation QA for sCT. Nevertheless, it is crucial to consider other QA aspects as well, such as sCT-to-CBCT or sCT-to-kV matching on an IGRT linac, end-to-end testing, and imaging QA for the MR scanner.

References

- Schneider U, Pedroni E, Lomax A. The calibration of CT Hounsfield units for radiotherapy treatment planning. *Phys Med Biol*. 1996;41:111–24.
- van Elmpt W, Landry G, Das M, Verhaegen F. Dual energy CT in radiotherapy: Current applications and future outlook. *Radiother Oncol*. 2016;119:137–44.
- Fonti R, Conson M, Del Vecchio S. PET/CT in radiation oncology. *Semin Oncol*. 2019;46(3):202209.
- Jonsson J, Nyholm T, Söderkvist K. The rationale for MR-only treatment planning for external radiotherapy. *Clin Transl Radiat Oncol*. 2019;18:60–5.
- Klüter S. Technical design and concept of a 0.35 T MR-Linac. *Clin Transl Radiat Oncol*. 2019;18:98–101.
- Raaymakers BW, Lagendijk JJW, Overweg J, Kok JGM, Raaijmakers AJE, Kerkhof EM, et al. Integrating a 1.5 T MRI scanner with a 6 MV accelerator: proof of concept. *Phys Med Biol*. 2009;54:N229–237.
- Spadea MF, Maspero M, Zaffino P, Seco J. Deep learning based synthetic-CT generation in radiotherapy and PET: A review. *Med Phys*. 2021;48:6537–6566.
- Han X. MR-based synthetic CT generation using a deep convolutional neural network method. *Med Phys*. 2017;44(4):1408–1419.
- Thorwarth D. Synthetic CT Generation for the Pelvic Region Based on Dixon-MR Sequences: Workflow, Dosimetric Quality and Daily Patient Positioning [Internet]. 2019; 23–7. Available from: https://marketing.webassets.siemens-healthineers.com/1800000006237915/e16f345fe7d9/siemens-healthineers-mreadings-mr-in-rt-edition-5-estro-complete-edition_1800000006237915.pdf
- Roberge D. Clinical Implementation and Evaluation of MR-only RT Planning for Brain Tumors [Internet]. 2020;18–23. Available from: https://marketing.webassets.siemens-healthineers.com/1800000007122162/242f1d75752b/MReadings-MR-in-RT_ESTRO_2020_1800000007122162.pdf
- Cabana J-F. MRI-only Based External Beam Radiation Therapy of Prostate Cancer [Internet]. 2021;24–34. Available from: https://marketing.webassets.siemens-healthineers.com/93284f54cf110e4c/98aebfdb8db9/sh-magnetom-world-MReadings_MR-in-RT_7th_Edition_2021.pdf
- Hoesl M. MR-based Synthetic CT. An AI-based Algorithm for Continuous Hounsfield Units in the Pelvis and Brain – with syngo.via RT Image Suite [Internet]. 2022 p. 30–42. Available from: https://marketing.webassets.siemens-healthineers.com/774bebe7e26ef699/35bffd2d66e1/siemens-healthineers_magneotm-world_MReadings_MR-in-RT_8th_Edition_ESTRO_2022.pdf
- Moore-Palhares D, Ho L, Lu L, Chugh B, Vesprini D, Karam I, et al. Clinical implementation of magnetic resonance imaging simulation for radiation oncology planning: 5 year experience. *Radiat Oncol*. 2023;18(1):27.
- Glade-Hurst CK, Paulson ES, McGee K, Tyagi N, Hu Y, Balter J, et al. Task group 284 report: magnetic resonance imaging simulation in radiotherapy: considerations for clinical implementation, optimization, and quality assurance. *Med Phys*. 2021;48(7):e636–e670.
- Dal Bello R, Lapaeva M, La Greca Saint-Estevan A, Wallimann P, Günther M, Konukoglu E, et al. Patient-specific quality assurance strategies for synthetic computed tomography in magnetic resonance-only radiotherapy of the abdomen. *Phys Imaging Radiat Oncol*. 2023;27:100464.
- Lapaeva M, La Greca Saint-Estevan A, Wallimann P, Günther M, Konukoglu E, Andratschke N, et al. Synthetic computed tomography for low-field magnetic resonance-guided radiotherapy in the abdomen. *Phys Imaging Radiat Oncol*. 2022;24:173–179.
- Besserer J, Cozzi L, Dipasquale G, Klöck S, Kunz G, Kurth C, et al. Quality control for Intensity-modulated radiation therapy. SSRMP Rec 15 [Internet]. 2007. Available from: <https://ssrpm.ch/wp-content/uploads/2014/08/r15imr-e.pdf>
- Karniadakis GE, Kevrekidis IG, Lu L, Perdikaris P, Wang S, Yang L. Physics-informed machine learning. *Nat Rev Phys*. 2021;3:422–440.



Contact

Riccardo Dal Bello, Ph.D.
Department of Radiation Oncology
University Hospital Zurich and
University of Zurich
Rämistr. 100
8091 Zurich
Switzerland
riccardo.dalbello@usz.ch

4D-MRI for Treatment Planning of Liver Tumors

Jessica Scholey¹; Horatio Thomas¹; Xin Miao²; Dianne Ferguson³; Mary Feng¹

¹Department of Radiation Oncology, University of California, San Francisco, CA, USA

²Siemens Medical Solutions USA Inc., Boston, MA, USA

³Department of Radiation Oncology, Brigham and Women's Hospital, Dana Farber Cancer Institute and Harvard Medical School, Boston, MA, USA

Introduction

Stereotactic body radiation therapy (SBRT) is increasingly being used to manage primary and metastatic liver tumors [1–3]. Accurately accounting for respiratory motion is imperative when targeting liver tumors with radiation. Strategies such as abdominal compression and breath-hold have been used to reduce tumor motion, though many patients cannot tolerate these strategies due to coexisting comorbidities and poor performance status. For these patients, four-dimensional computed tomography (4D-CT) is used to estimate tumor motion throughout the respiratory cycle and generate internal target volumes (ITVs) for radiotherapy treatment planning. However, delineating liver tumors on 4D-CT is very challenging because of its inherent poor soft tissue contrast. These tumors can only be visualized using intravenous contrast, which is eliminated from the liver quickly, creating practical challenges in correctly timing contrast administration with image acquisition. Contrast-enhanced 4D magnetic resonance imaging (4D-MRI)¹ offers a promising strategy for directly visualizing liver tumor motion. The superior soft tissue contrast of MRI and long usable duration of hepatobiliary MRI contrast allows the visualization of tumors throughout the respiratory cycle [4,5].

Prior studies have demonstrated 4D-MRI acquisition using multi-slice 2D or 3D sequences with Cartesian or non-Cartesian sampling trajectories [6–10]. Despite

increased interest, clinical implementation of 4D-MRI technology has been limited because it requires specialized acquisition protocols, reconstruction techniques, and hardware. In this study, we adopted a novel 4D-MRI technique¹ that performs continuous volumetric scanning with self-gating and retrospective respiratory binning that can capture irregular respiratory motion. We assessed the feasibility of using 4D-MRI in target volume generation for liver tumors and compared 4D-MRI with 4D-CT in terms of liver tumor clarity and the dosimetry of radiation treatment plans [11].

Materials and methods

Image acquisition and reconstruction

Twelve patients undergoing SBRT to the liver were prospectively recruited into this IRB-approved study. All patients received same-day 4D-CT and 4D-MRI simulation using identical positioning and immobilization. 4D-CT scans were acquired over a single respiratory cycle (120 kVp, 0.98 × 0.98 mm voxels, 3 mm slice thickness, scan time ~1 minute) and retrospectively binned using 8-phase reconstruction (SOMATOM Definition AS, Siemens Healthcare, Forchheim, Germany).

MRIs were acquired on a 3 Tesla MRI simulator (MAGNETOM Vida, Siemens Healthcare, Erlangen,

¹Work in progress. The application is currently under development and is not for sale in the U.S. and in other countries. Its future availability cannot be ensured.

Germany) using a large 18-channel UltraFlex coil suspended from a coil bridge and a 32-channel spine coil. 4D-MRIs were acquired after injection with hepatobiliary contrast (gadoxetic acid) [12] using a T1-weighted 3D fast gradient echo sequence acquired in the axial plane with a golden-angle stack-of-stars sampling trajectory (TE/TR = 1.4/2.8 ms, 1.3×1.3 mm voxels, 3 mm slice thickness, FOV = 380×380 mm², 64–72 slices) [13]. 4D-MRI *k*-space was filled continuously over multiple respiratory cycles (scan time ~8–10 minutes). A self-gating signal (SGS) was extracted from the *k*-space center and used as a respiratory motion surrogate. The Advanced 4D MRI¹ research sequence was used to provide a binning option that separates inhalation and exhalation in the SGS-based motion trace. For consistency with CT, the total number of respiratory bins was chosen as 8. The SGS waveform was first segmented into 4 amplitude bins, and then data in the same bin were separated into inspiration and expiration groups according to the direction of the motion. After respiratory binning, images were reconstructed using a standard radial re-gridding algorithm.

To identify regular and irregular breathers, breathing regularity was quantified using the SGS waveform. The peak-to-trough range and mid-level amplitude (i.e. (peak-amplitude + trough-amplitude) / 2) were calculated for each respiratory cycle. The average mid-level amplitude across all cycles normalized by the average peak-to-trough range was used as the regularity score. Subjects with the score greater than 20% were defined as irregular breathers.

Image analysis

Image quality was assessed using a 4-point Likert scale ('clarity score'). Images were scored as follows:

- 1 diagnostic quality,
- 2 non-diagnostic, but clearly demarcated lesion,
- 3 less clear borders but definable for treatment planning, and
- 4 lesion undefinable for treatment planning.

Images for each patient were reviewed concurrently by two radiation oncologists and a consensus score was assigned for the end-inspiration and end-expiration phase of each binning technique. Paired *t*-tests were used to compare images and differences were considered statistically significant if *p*-value < 0.05.

Radiotherapy target delineation and treatment planning

Targets were independently contoured on the 4D-CT and 4D-MRI scans by two radiation oncologists. Gross target

volumes (GTV) were contoured on each image phase and internal target volumes (ITV) were generated by summing the GTVs. Planning target volumes (PTVs) were generated by expanding ITVs 8 mm vertically and 5 mm in all other directions. Volumetric information for MR- and CT-derived PTVs were extracted and compared using paired *t*-tests.

4D-CT and 4D-MRI datasets were co-registered by fusing ITVs in the corresponding end-expiration phases. For patients with multiple lesions, separate registrations were performed for each target to account for liver compressibility and rotation. For each patient, a planning CT was generated from the mean intensity projection of the 4D-CT images. All PTVs were transferred to, and OARs were contoured on, this average 4D-CT dataset. To assess dosimetric impacts of MR-derived (PTV_{MR}) and CT-derived (PTV_{CT}) targets, radiation plans were optimized separately on each dataset according to the target prescription and OAR objectives used clinically for each patient.

Treatment planning was performed in RayStation (v.7.0 RayStation Laboratories, Stockholm, Sweden) using 10 MV or 10 FFF photon coplanar volumetric modulated arc therapy. Targets were treated to a median dose of 50 Gy in 5 fractions. To maintain consistency and ensure plan quality, all plans were created by a single planner who followed the same workflow that is implemented for clinical patients. To minimize the introduction of biases towards MR- versus CT-optimized plans, each patient's plan was initialized using the same beam orientation and optimization objectives. Thereafter, objectives were adjusted independently during plan optimizations to produce clinically acceptable plans. The proportion of the PTVs receiving 90% of the prescription dose for MR- and CT-derived targets was extracted from the plans optimized for the respective targets. To assess the MR target coverage using CT-optimized plans used in current practice, the PTV coverage for the MR-derived targets was also extracted from the CT-optimized plan. The PTV coverage for MR-derived targets on the MR- and CT-optimized plans were compared to the coverage of CT-derived targets using paired *t*-tests.

Results

Image acquisition

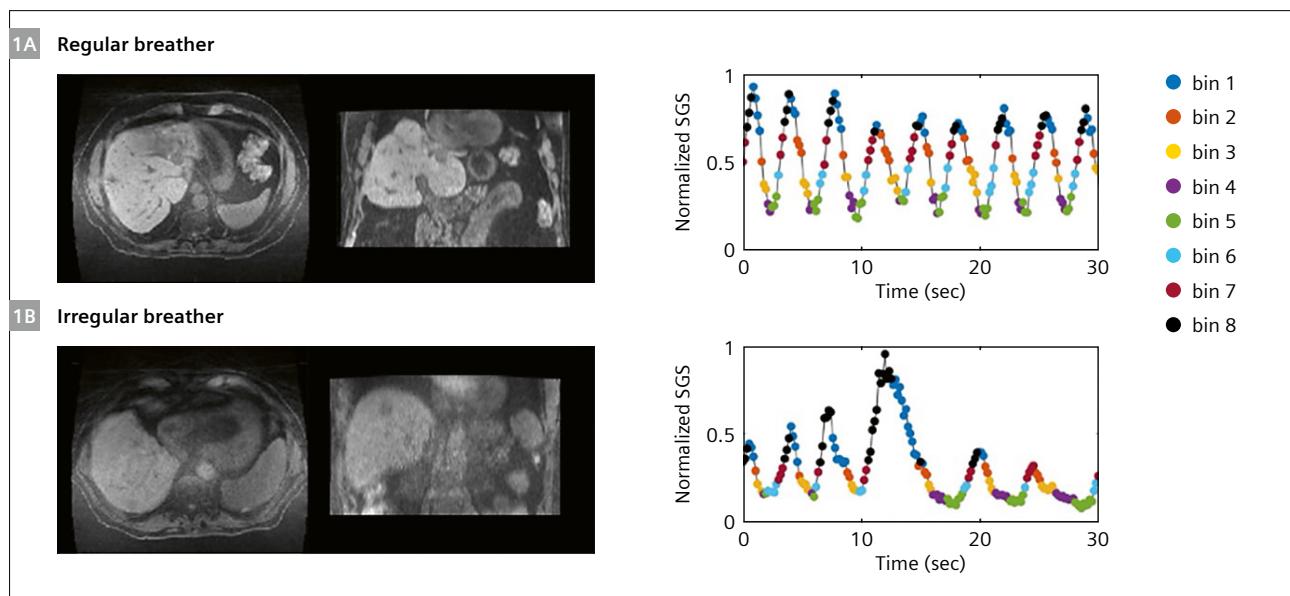
4D-MRIs were obtained for twelve patients with a total of 17 liver tumors. Of the twelve patients, six were classified as regular breathers and six as irregular breathers. Example axial and coronal views of regular and irregular breathers is shown in Figure 1, along with their corresponding respiratory traces and binning results. The binning algorithm was

found to be robust to both regular (Fig. 1A) and irregular (Fig. 1B) breathing patterns.

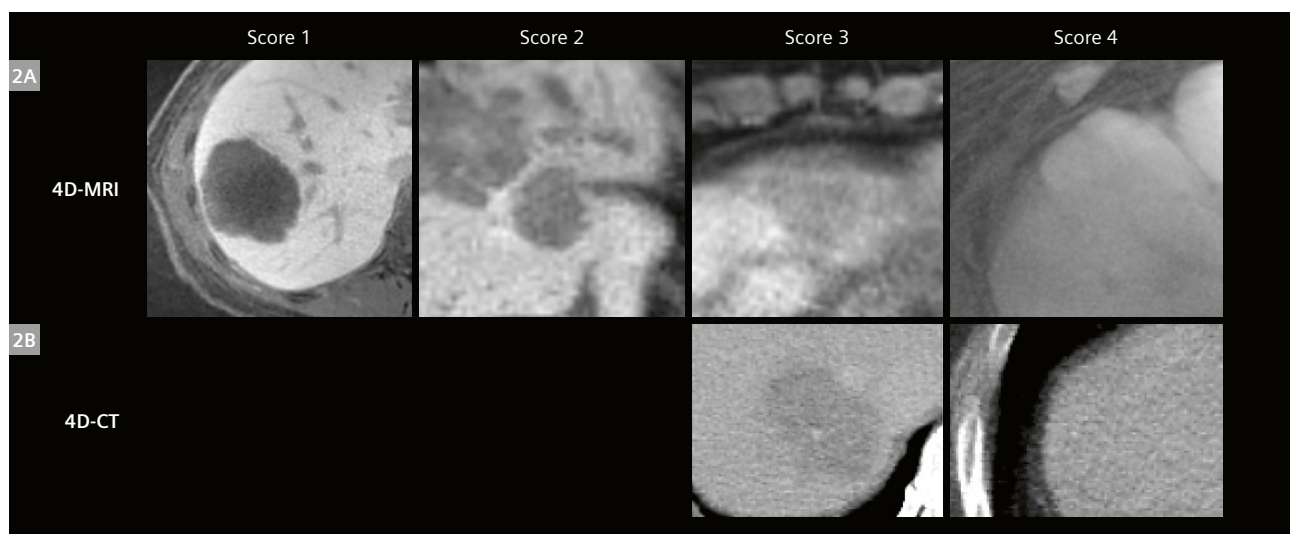
Image quality was assessed using a 4-point clarity score, with lower clarity scores corresponding to superior image quality, as shown in Figure 2. Clarity scores were significantly better for 4D-MRI versus 4D-CT (1.2 ± 0.4 and 3.5 ± 0.7 , respectively, $p < 10^{-9}$). No liver tumors were rated 4 on any 4D-MRI because all lesions were definable on all phases regardless of the binning algorithm. No liver tumors were rated 1 or 2 on any 4D-CT.

Radiotherapy target delineation and treatment planning

On average, there was no significant difference between volumes of MRI-derived and CT-derived targets (39 cc vs. 44 cc, respectively, $p = 0.44$). Analysis of the radiation plans revealed no significant difference between the dosimetric coverage of 17 CT-derived and MR-derived PTVs on the plans optimized for their respective volumes (PTV receiving 90% of prescription: 89.38% vs. 90.61%, respec-



1 Comparison of images and respiratory binning for patients who breathed **(1A)** regularly and **(1B)** irregularly. A 30-second segment of the respiratory self-gating signal (SGS) is also displayed for each binning option. Each point in the waveform has a timing correspondence to a segment of *k*-space data acquisition, and the color represents the bin index assigned to the data.



2 Atlas depicting the Likert-4 scale qualitative assessment of image quality of tumors on 4D-MRI **(2A)** and 4D-CT **(2B)** reconstructions. Score legend: (1) diagnostic quality, (2) non-diagnostic, but clearly demarcated lesion, (3) less clear borders but definable for treatment planning, and (4) lesion undefinable for treatment planning. There were no 4D-CT images scored at values of 1 or 2.

tively, $p = 0.68$) demonstrating similar plan quality for the targets. However, a comparison of the PTV coverage on the CT-optimized plan revealed significantly lower coverage of MR-derived compared to CT-derived targets (PTV receiving 90% of prescription: 75.56% vs. 89.38%, $p = 0.002$), indicating that planning to the 4D-CT-derived target would result in underdosing of the tumor (Fig. 3). There was no significant difference in the mean liver dose including the PTVs (16.34 Gy vs. 15.2 Gy, respectively, $p = 0.29$) or the doses to additional organs at risk for CT- and MR-optimized plans ($p > 0.05$), as OAR sparing had priority over target coverage.

Discussion

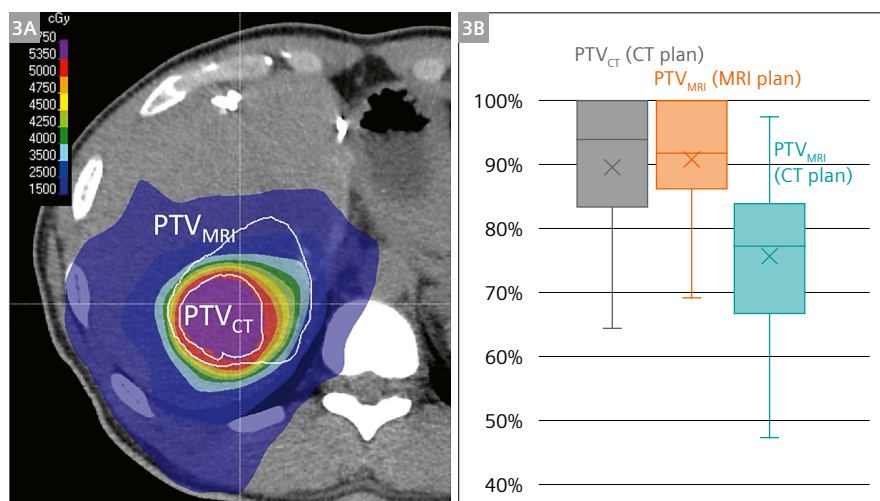
Accurately delineating liver tumors is essential for delivering radiation dose to the desired targets while minimizing radiation to normal tissues. In this study, we demonstrate the feasibility of using contrast-enhanced 4D-MRI for the direct visualization of liver tumors throughout the respiratory cycle for ITV generation. Estimating the motion of liver tumors on 4D-CT is fraught with uncertainty because detailed internal anatomy cannot be seen. In contrast, the reliable direct visualization of liver tumors during the respiratory cycle using 4D-MRI facilitates the production of ITVs that accounts for respiratory hysteresis and tissue compressibility.

We adopted a 4D-MRI technique that performs continuous volumetric scanning with self-gating and respiratory binning using a 3D T1-weighted fast gradient echo sequence and a golden-angle radial acquisition scheme. This acquisition scheme is inherently more robust to motion artifacts compared to Cartesian acquisition and allows high-frequency sampling of the center of k -space, from which a respiratory motion trace can be derived. As the motion trace is extracted from the acquired data itself, there is no need for external respiratory devices or

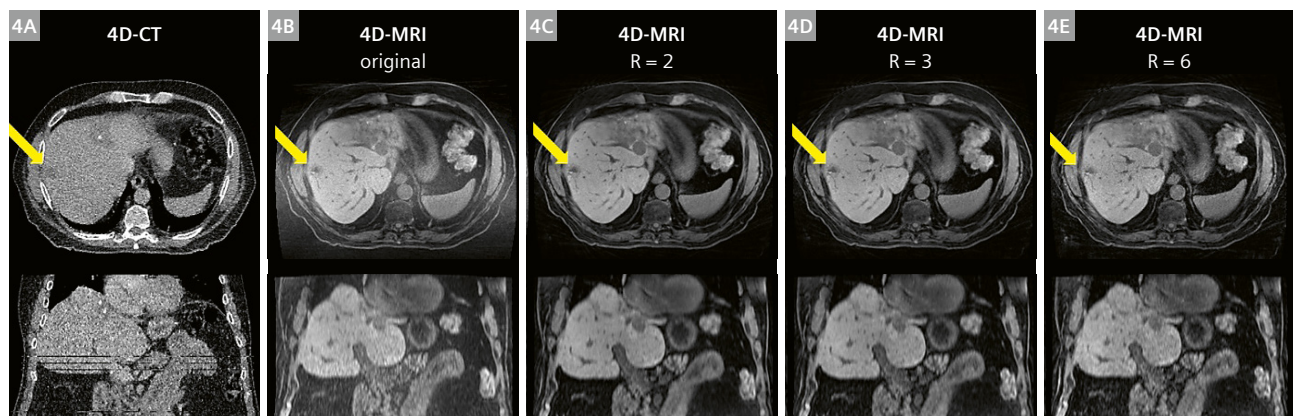
surrogates. In contrast to 4D-CT acquisition, which acquires data through a single respiratory cycle, this 4D-MRI approach continuously samples breathing over several minutes, with the final average over multiple respiratory cycles potentially being more representative of patients' normal breathing versus helical 4D-CT.

The dosimetric data demonstrated that the use of 4D-MRI may improve radiation targeting of liver tumors. In our study, MRI-generated ITVs tended to be smaller than CT-derived ITVs, although the difference was not statistically significant. Dosimetric data for radiation plans showed similar coverage when optimized for CT-derived and MR-derived targets and dose to adjacent organs at risk, though the significantly lower MR-derived target coverage on CT-optimized plans suggests that the current methods of treatment planning may lead to tumor underdosing and increase the risk of marginal misses. It is unclear how much the difference in ITV generation contributes to the local recurrence of tumors after SBRT, as tumor control is generally high ($> 90\%$) but recurrences could be due to marginal misses resulting from the under-contouring of tumor positions during respiration. Additional research is needed on the clinical impact using MR-based targets on tumor control and tissue toxicity.

Reducing MRI acquisition time is advantageous for many reasons including increased patient comfort and hospital throughput. One method for MRI acceleration is through compressed sensing (CS), however, the effects of CS acceleration on 4D-MRI in the context of radiotherapy treatment planning has not yet been investigated. Our group is investigating the compressed sensing capabilities currently available in the Advanced 4D MRI research sequence. Figure 4 shows example axial and coronal views of a (4A) 4D-CT, (4B) original 4D-MRI (~10-minute acquisition), and simulated 4D-MRI acceleration rate (R) of (4C) $R = 2$ (~5-minute acquisition), (4D) $R = 3$ (~3.3-minute acquisition), and (4E) $R = 6$ (~1.7-minute acquisition).



3 (3A) Example axial slice of a radiation treatment plan optimized using CT-derived target volume ('CT plan'). The inner white line shows the CT-derived target (PTV_{CT}), the outer white line shows the MR-derived target (PTV_{MRI}), and the colored regions correspond to isodose lines. (3B) A boxplot distribution for all 17 PTVs covered by 90% of the prescription dose shows a similar distribution of PTV coverage between CT-derived (gray) and MR-derived (orange) targets on plans optimized for their respective volumes and lower coverage of MRI-derived (petrol) targets for CT-optimized plans.



4 Example axial and coronal slices of exhale phase **(4A)** 4D-CT and 4D-MRIs reconstructed using **(4B)** original 3000 spoke sampling and acceleration factors (R) **(4C)** R = 2, **(4D)** R = 3, and **(4E)** R = 6. The liver tumor is annotated using the yellow arrow in all axial planes. Note that the 4D-MRI improves tumor contrast and resolves respiratory-induced motion artifacts relative to the 4D-CT.

Overall, there are many factors that can impact 4D-MRI image quality, including the breathing pattern of the subject, choices of sparsity constraints and regularization weighting in the CS algorithm, and SGS signal processing. The impacts of these factors are currently being investigated using a 4D MRI motion phantom.

Conclusion

This study demonstrates the feasibility of using hepatobiliary contrast-enhanced 4D-MRI to delineate gross liver tumors directly throughout the respiratory cycle. The lower coverage of directly visualized MRI targets in plans generated using standard of care 4D-CT-derived targets suggests that the adoption of 4D-MRI for motion management may improve radiation treatment of liver lesions and reduce the risk of marginal misses. Future investigations will focus on impacts of compressed sensing acceleration and ground-truth measurements in a 4D-MRI phantom.

References

- 1 Mahadevan A, Blanck O, Lanciano R, et al. Stereotactic Body Radiotherapy (SBRT) for liver metastasis – clinical outcomes from the international multi-institutional RSSearch® Patient Registry. *Radiation Oncology*. 2018;13(1):1-11.
- 2 Ohri N, Tomé WA, Romero AM, et al. Local control after stereotactic body radiation therapy for liver tumors. *International Journal of Radiation Oncology* Biology* Physics*. 2021;110(1):188-195.
- 3 Doi H, Beppu N, Kitajima K, Kuribayashi K. Stereotactic body radiation therapy for liver tumors: current status and perspectives. *Anticancer Research*. 2018;38(2):591-599.
- 4 Wojcieszynski AP, Rosenberg SA, Brower JV, et al. Gadoxetate for direct tumor therapy and tracking with real-time MRI-guided stereotactic body radiation therapy of the liver. *Radiother Oncol*. Feb 2016;118(2):416-8. doi:10.1016/j.radonc.2015.10.024
- 5 Leyendecker JR. Gadoxetate disodium for contrast magnetic resonance imaging of the liver. *Gastroenterology & Hepatology*. 2009;5(10):698.
- 6 von Siebenthal M, Szekely G, Gamper U, Boesiger P, Lomax A, Cattin P. 4D MR imaging of respiratory organ motion and its variability. *Physics in Medicine & Biology*. 2007;52(6):1547.
- 7 Hu Y, Caruthers SD, Low DA, Parikh PJ, Mutic S. Respiratory amplitude guided 4-dimensional magnetic resonance imaging. *International Journal of Radiation Oncology* Biology* Physics*. 2013;86(1):198-204.
- 8 Tryggstad E, Flammang A, Han-Oh S, et al. Respiration-based sorting of dynamic MRI to derive representative 4D-MRI for radiotherapy planning. *Medical physics*. 2013;40(5):051909.
- 9 Deng Z, Pang J, Yang W, et al. Four-dimensional MRI using three-dimensional radial sampling with respiratory self-gating to characterize temporal phase-resolved respiratory motion in the abdomen. *Magnetic resonance in medicine*. 2016;75(4):1574-1585.
- 10 Van de Lindt TN, Fast MF, van der Heide UA, Sonke J-J. Retrospective self-sorted 4D-MRI for the liver. *Radiotherapy and Oncology*. 2018;127(3):474-480.
- 11 Thomas HR, Miao X, Ferguson D, et al. Contrast-enhanced 4D-MRI for internal target volume generation in treatment planning for liver tumors. *Radiotherapy and Oncology*. 2022;
- 12 Van Beers BE, Pastor CM, Hussain HK. Primovist, Eovist: what to expect? *Journal of hepatology*. 2012;57(2):421-429.
- 13 Grimm R, Block K, Hutter J, et al. Self-gating reconstructions of motion and perfusion for free-breathing T1-weighted DCEMRI of the thorax using 3D stack-of-stars GRE imaging. 2012:3814.

Contact

Jessica Scholey, Ph.D., DABR
Assistant Professor
Director of MRI Simulation
Department of Radiation Oncology
University of California San Francisco
505 Parnassus Ave., Room L-75
San Francisco, CA 94143-0226
USA
Tel.: +1 (415) 353-7191
jessica.scholey@ucsf.edu



Put the advantages of the MAGNETOM World to work for you!

www.siemens-healthineers.com/magnetom-world-rt

Siemens Healthineers' global MRI community offers peer-to-peer support and information. Radiation Oncologists, Radiologists, Medical Physicists, Technologists and Cardiologists have all contributed with publications, presentations, training documents, videos, case studies and more – all freely available to you via this unique network.

MRI in Radiation Therapy

Peer-to-peer exchange of protocols, articles and tips

Protocols

Application Tips

Articles & Case Studies

Talks & Videos

Contact Us

Don't miss the MRI protocols and practical tips and tricks for several body regions from experts for both experts and novice users. The information can help in supporting your entire clinical team and grow your practice.

The centerpiece of the MAGNETOM World Internet platform consists of MAGNETOM users' results. Here you will find articles, case reports and application tips allowing you to optimize your daily work.

MR-integrated Workflows in Radiation Therapy

for MAGNETOM Systems

Not for distribution in the US

Second
extended
edition

Eric Paulson, Ph.D.
Medical College of Wisconsin, Milwaukee, USA

Yue Cao, Ph.D.
University of Michigan, Ann Arbor, USA

Leah Best
Calvary Mater Hospital, Newcastle, NSW, Australia

Trina Herbert
The Royal Marsden NHS Foundation Trust,
Sutton, UK

Maja Sohlén, Ph.D.
Sahlgrenska University Hospital, Gothenburg,
Sweden

Robba Rai, MHLthSc and Gary Liney, Ph.D.
Liverpool and Macarthur Cancer Therapy Centre,
Ingham Institute for Applied Medical Research,
Sydney, Australia

Cynthia Ménard, M.D., FRCPC
and David Roberge, M.D., FRCPC
Centre hospitalier de l'Université de Montréal,
Canada



Evaluation of the Contour 24 Coil for an MR-Only Radiotherapy Workflow

Emma Doran, Stefanie Thomson, Marimuthu Sankaralingam

Radiotherapy Physics, Beatson West of Scotland Cancer Centre, DCPB, NHS GGC, Glasgow, UK

Introduction

The Contour 24 receive coil is flexible, lightweight, and should not influence the patient's body contour during scanning. This makes it an attractive radiotherapy imaging solution compared to the rigid setups offered by a rigid coil and bridge frame.

In this study, we compare the image quality and geometry parameters calculated from MR images of an ACR MR phantom acquired using the Body 18 coil (a traditional rigid design) and the Contour 24 coil. The aim was to investigate any difference in performance of the two coil solutions. Following this, the effect of the Contour 24 coil on the patient's body contour was evaluated using MR images acquired as part of a project evaluating the synthetic CT (sCT) Dixon sequence available on the 1.5T MAGNETOM Sola RT Pro Edition, an MRI RT simulator (Siemens Healthineers, Erlangen, Germany). The Contour 24 coil was placed anteriorly over the pelvic region of

eight prostate patients for the full scan protocol, which lasted approximately 20 minutes (Fig. 1).

The prostate patients included in this study also received a planning CT scan, which was used to generate the treatment plan and for dose calculation. In order to compare the body contour generated for the planning CT with the body contour generated for the sCT, the CT image data was used as the gold standard. The aim was to confirm that the Contour 24 coil had no effect on the sCT body contour by assessing its similarity to the planning CT body contour, and to demonstrate that the sCT can be used reliably for dose calculation in an MR-only workflow.

Methods

The image quality and geometry results from the weekly QA using the ACR MR phantom were studied retrospectively. A different receive coil is tested each week, providing 10



- 1 The Contour 24 coil is placed anteriorly over the pelvic region of the patient. The coil is flexible enough to rest comfortably over the patient like a blanket.

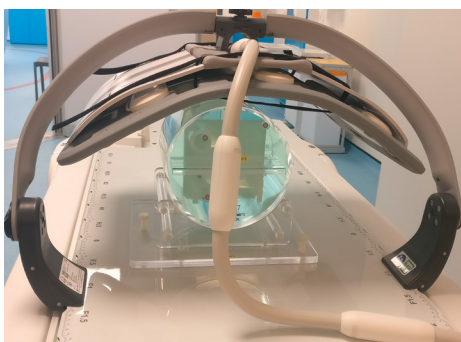
sets of results for the Body 18 coil and 16 sets of results for the Contour 24 coil. The experimental setups used in the QA are provided in Figure 2 and show the coil bridge that is used in conjunction with the Body 18 coil. T1- and T2-weighted axial images of the phantom are acquired according to the protocol outlined in the ACR Quality Control Manual using either the Body 18 or the Contour 24 coil and the Spine Coil located within the scanner bed. The image quality and geometry results were calculated using MR AutoQA Plus software (version 1.7.6.7, QA Benchmark LLC, Maryland, USA) on both T1- and T2-weighted images. They include high-contrast spatial resolution, slice thickness accuracy, slice position accuracy, geometric accuracy, image intensity uniformity, ghosting, signal-to-noise ratio (SNR), and low-contrast detectability. The average and standard deviation of each of these results were calculated and used to compare the performance of the coils. The similarity between the body contours generated for an sCT and a planning CT acquired for eight prostate patients was evaluated. The body contour was generated using the Search Body tool in Eclipse's Contouring Workspace (Varian, a Siemens Healthineers Company, Palo Alto, CA, USA) with a lower threshold of -350 HU to detect the body's outline. Default post-processing

parameters were used (Number of Largest Parts = 1, Disconnect Radius = 0.2 cm, Fill All Cavities = 2-D All, Close Openings Radius = 0.2 cm, Smoothing Level = 3). The planning CT body contour was copied onto the sCT dataset via a rigid registration between the planning CT and the underlying Dixon images used to generate the sCT. Both planning CT and sCT body contours were cropped superiorly and inferiorly, encompassing the region from the bottom of the ischial tuberosities to L5 (see Fig. 3). This corresponds to the area of interest over which the Contour 24 coil is placed during imaging.

The Boolean Operator tool was used to create an additional structure that included the volume common to both planning CT and sCT body contours. The volumes of the common structure, cropped CT body, and cropped sCT body contours were recorded and the Dice similarity coefficient (DSC) was calculated as follows:

$$DSC = \frac{(2 \times \text{Volume}_{\text{COMMON}} [\text{cm}^3])}{(\text{Volume}_{\text{CT BODY}} [\text{cm}^3] + \text{Volumess}_{\text{CT BODY}} [\text{cm}^3])}$$

Mean and standard deviation DSC values were also calculated, and any outliers were investigated.

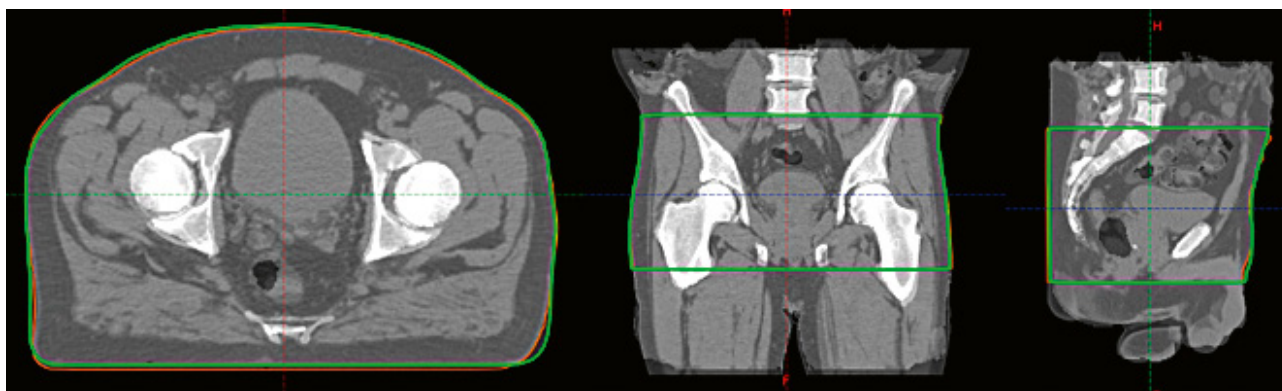


Body 18 + Spine Coil setup



Contour 24 + Spine Coil setup

- 2** Setups for the weekly QA with the ACR MR phantom for the Body 18 and Contour 24 coils. A bridge frame is used with the Body 18 coil to hold the coil over the phantom. Images are also acquired using the Spine Coil located along the length of the scanner bed.



- 3** Body contours generated by the planning CT (orange) and the sCT (green) were cropped to relevant patient anatomy prior to DSC calculation.

QA result	Expected result	T1-weighted images		T2-weighted images	
		Contour 24 coil	Body 18 coil	Contour 24 coil	Body 18 coil
High-contrast spatial resolution	$\leq 1 \text{ mm}$	1.0 mm	1.0 mm	1.0 mm	1.0 mm
Slice thickness accuracy	$5 \pm 0.7 \text{ mm}$	5.0 mm	4.9 mm	4.4 mm	4.4 mm
Slice position accuracy	$0 \pm 5 \text{ mm}$	0.5 mm	0.3 mm	0.5 mm	0.3 mm
Geometric accuracy	$190 \pm 2 \text{ mm}$	190.5 mm	190.2 mm	190.6 mm	190.2 mm
Image intensity uniformity	$\geq 87.5\%$	96.7%	95.4%	96.6%	96.6%
Ghosting	≤ 0.025	0.001	0.004	0.002	0.005
SNR	Baseline	341	237	301	200
Low-contrast detectability	Spokes $T1 \geq 30$ $T2 \geq 25$	34	34	33	34

Table 1: Average QA results calculated from T1 and T2 data acquired with the Contour 24 and Body 18 coils.

Results

The average QA results calculated from the trending data of weekly QA are presented in Table 1. Most of the image-quality and geometry results from T1- and T2-weighted images acquired with the Body 18 and Contour 24 coils were similar, with slice thickness accuracy, slice position accuracy, geometric accuracy, image intensity uniformity, and ghosting showing improvement with the Contour 24 coil. The Contour 24 SNR was 44% (T1w) and 51% (T2w) higher than the Body 18 SNR.

DSC values calculated for each patient are listed in Table 2. The mean DSC calculated across all eight subjects was 0.979 with a standard deviation of 0.006. The difference in volume between the sCT BODY and CT BODY structures ranged from -5.57% (larger sCT BODY) to +1.12% (larger sCT BODY).

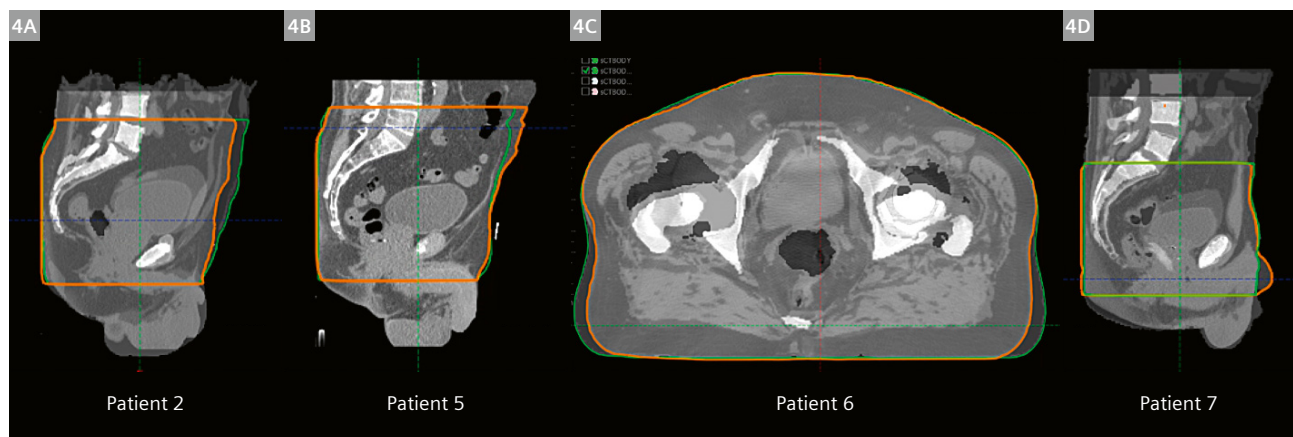
Discussion

Both the Body 18 and Contour 24 coils have similar image quality and geometry performance when assessed using the ACR MR phantom. The image SNR is higher in the images acquired with the Contour 24 coil, probably because of its closer proximity to the phantom. The lower SNR achieved with the Body 18 coil demonstrates the downside of having to use a bridge frame to avoid altering the patient's body contour in a rigid coil setup.

Patient Number	DSC
1	0.984
2	0.968*
3	0.982
4	0.986
5	0.977*
6	0.981*
7	0.978*
8	0.985

Table 2: Dice similarity coefficients calculated for each patient.

The lower DSC scores for patients 2, 5, 6, and 7 were investigated and found to be related to anatomical and positioning variations between the planning CT and sCT. Patient 2 had significant bladder distension in the sCT, causing anterior extension of the sCT body contour. Patient 5 had anteriorly located gas in the planning CT, which also caused anterior expansion of the upper abdomen and subsequently the CT body contour. Patient 6 had different



4 Patients 2, 5, 6, and 7 had lower DSC scores that were related to anatomical and positioning variations between the planning CT and sCT: **(4A)** bladder distension in sCT led to anterior extension of the sCT body contour; **(4B)** anterior gas led to anterior expansion of the upper abdomen and subsequently the CT body contour; **(4C)** this patient with bilateral hip prostheses had different posterior fat distribution between CT and MRI scans, which led to a larger sCT body contour in the posterior area of interest for the analysis; **(4D)** different anatomical positioning between CT and MRI scans led to an extended CT body contour to the inferior of the region of interest in this study.

posterior fat distribution between planning CT and MRI scans, which caused a larger sCT body contour in the posterior area of interest for the analysis. Patient 7 was positioned slightly differently between planning CT and MRI scans, causing an extended CT body contour toward the inferior of the region of interest for this study.

Patient 6 also had bilateral hip prostheses, and the images show that image quality degradation is localized to the implant and has no significant effect on the patient's overall anatomy/body contour.

Conclusion

The Contour 24 coil provided superior SNR results when calculated from T1- and T2-weighted phantom images. This is an advantage of being able to place the flexible coil directly onto the object being imaged. Better SNR is an advantage in MR imaging and provides higher quality images for contouring, sCT generation, and functional imaging in MR-only radiotherapy workflows.

Using DSC as a quantitative measure of similarity, a comparison between planning CT-generated body contours and sCT-generated body contours showed that the Contour 24 coil does not significantly alter the patient contour during MRI scanning. In addition to being a lightweight and flexible receive coil that can conform to the patient's anatomy to provide higher image SNR, the Contour 24 coil is an ideal solution for MRI scanning in radiotherapy

imaging applications. The results of this study provide confidence that sCT geometry accurately reflects that of the planning CT geometry within the clinical region of interest and could be used for dose calculation in MR-only planning.

Acknowledgments

We would like to acknowledge the following RT-MR radiographers, who make up the MR-Sim team: Cave Sharon, Kay Nisbet, and Kirsty Brown.

Contact

Marimuthu Sankaralingam, M.Sc. (Med.Phys)
Head of Radiotherapy Imaging
Radiotherapy Physics
Beatson West of Scotland Cancer Centre
1053 Great Western Road
Glasgow G12 0YN
United Kingdom
marimuthu.sankaralingam@ggc.scot.nhs.uk

A Breast MR-in-RT Workflow: Motion Assessment of Breast and OAR with 4D Self-Gating MRI

Sylvain Doussin, Ph.D.; Melanie Habatsch; Manuel Schneider, Ph.D.; Martin Requardt, Ph.D.

Siemens Healthineers, Erlangen, Germany

Introduction

Breast cancer is the most common cancer among women [1]. Recently, in addition to computed tomography (CT), soft-tissue MRI has been used to support image-guided RT plans for breast cancer patients. For CT imaging, breast cancer patients are immobilized in supine and prone position [2]. However, diagnostic breast MRI is typically performed in a prone patient setup, which can lead to mismatch and registration errors. In the present work, we propose a novel RT planning workflow for breast cancer patients with free-breathing (FB) MRI measurements in supine position (Fig. 1) and evaluation of motion in the breast and organs-at-risk (OAR), without external surrogates for respiration, using a 4D respiratory self-gating (4D MRI) sequence. We also assessed image quality for organ depiction for contouring.



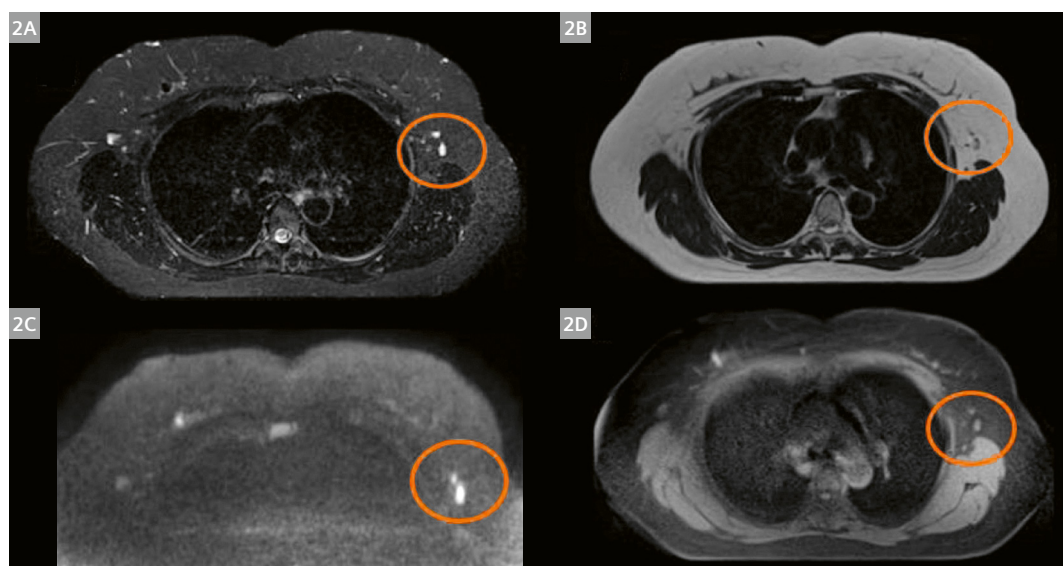
1 Supine patient setup with coil in the MRI scanner.

Methods

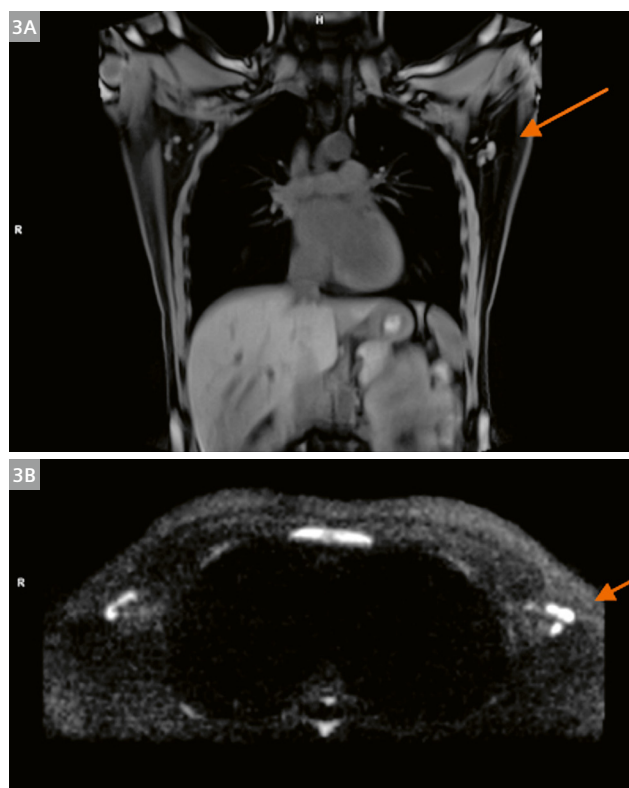
The proposed workflow uses the Qfix® (Avondale, AZ, USA) breast board including arm holders, and the Qfix® coil holder (RT-4546 Access Supine MR Breast Device, RT-4546AA-01 Access Arm Support, RT-4546AW-01 Access Wrist Support) on a 1.5T scanner (MAGNETOM Sola, Siemens Healthcare, Erlangen, Germany) in combination with body array (anterior) and 48-channel spine (posterior) coils.

Both arms were positioned overhead (Fig. 1) to minimize the distance between the patient's surface and the 18-channel body array coil, which would increase the signal-to-noise ratio (SNR). No compression, no stereotactic mask, no laser, and no marking devices were used. Five healthy female volunteers were enrolled ($n = 5$; age: 56 ± 9 years; weight: 68 ± 17 kg; height: 167 ± 7 cm). We performed routine clinical diagnostic protocols for the breast, including T2w, T2w STIR, and RESOLVE DWI with free breathing (Figs. 2, 3) in the treatment position.

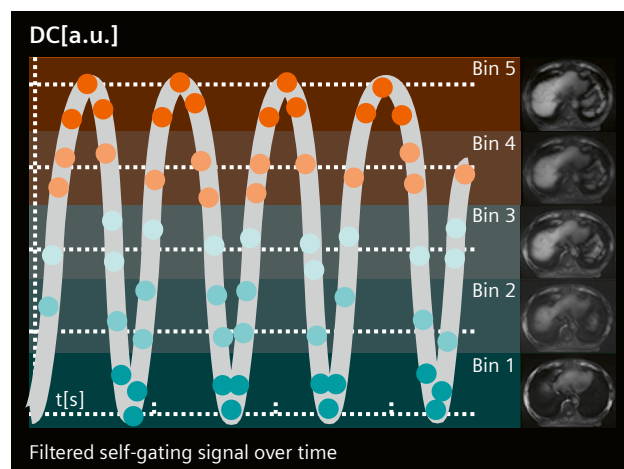
In addition, we asked the volunteers for a deep inspiration breath-hold (DIBH) to acquire a 3D GRE (VIBE Dixon, Fig. 2D) that we could compare with the 4D MRI. The 4D MRI is a self-gating respiration-resolved radial 3D GRE sequence and we have optimized the contrast for OAR contouring. The 4D MRI protocol was optimized to reduce the streak artifacts inherent to radial acquisitions by adapting the number of radial views. Images are automatically binned, or sorted, into discrete phases that correspond to a patient's distinct respiratory motion (Fig. 4). A respiratory self-gating signal was extracted from the central k -space samples and used as a respiratory surrogate signal.



2 Diagnostic scans:
(2A) T2 STIR,
(2B) T2W TSE,
(2C) RESOLVE
diffusion b800,
(2D) T1 VIBE
Dixon.



3 Lymph node depiction in coronal and axial orientation, visible here with 4D MRI average coronal (3A) and diffusion-weighted RESOLVE SPAIR b800 transversal (3B).



4 4D MRI: T1 StarVIBE respiratory self-gating (RSG); stack-of-stars trajectory with radial in-plane sampling acquired with golden-angle and cartesian partition encoding [3].

Motion of the target volume and OAR was assessed over seven phase bins, with 3500 radial views. 4D MRI was applied in axial orientation from jugulum to liver, and in coronal orientation from nipple to posterior lung lobes (each with TE 2.46 ms, TR 3.6 ms, FA 10°,

FOV 420 × 420 mm, matrix 288 × 288, slice thickness 3 mm, 64 slices, TA 8:35 min, slab-selective excitation, 890 Hz/pixel). In addition to the seven bin images, an average image was reconstructed (Fig. 5C).

Organ motion in free breathing was quantified by measuring the minimum distance between the heart (OAR) and chest wall at end-of-exhale, at end-of-inhale, and in DIBH [4]. In addition, the anterior-posterior and lateral relative OAR motion (OAR movement between inhale and exhale) for the heart and chest wall were assessed [5].

Results

Patient positioning in supine takes less than five minutes and improves patient comfort compared to prone position.

Despite a greater distance between body surface and body coil, high clinical image quality was achieved for all contrasts (Figs. 2, 3, 5) for potential lesion detection [6]. Although for all contrasts, the same number of lymph nodes was visible (Fig. 2) in the axillary region, including with the RESOLVE diffusion technique [6]. The heart, ribs, breasts, liver, pancreas, aorta, muscles, soft tissue, spleen, stomach, and spine could be contoured with 4D MRI (Figs. 5, 6) and clinical weighted images.

We observed negligible chest movement between FB exhale and FB inhale (0.1 ± 0.1 cm, Table 1). This small amplitude might be due to the patient's arms-up positioning. We also observed very little chest motion when volunteers were positioned and breathing freely.

The OAR motion is clearly in the head-feet direction. The distance between chest wall and heart was measured on transversal images with the nipple in the views. The heart has limited right-to-left motion between end-of-inhale and end-of-exhale (0.3 ± 0.1 cm). To assess the reproducibility of the patient setup, we measured the same volunteer twice at a one-day interval. We found very similar organ positions and movements in the two scans: The heart–chest wall distance in axial views was 1.6 ± 0.5 cm, 1.9 ± 0.1 cm, and 2.1 ± 0.8 cm for FB exhale, FB inhale, and DIBH, respectively.

With 170 breathing cycles per bin, the 4D MRI strongly reduces the impact of irregular breathing on image quality compared to 4D CT acquisition.

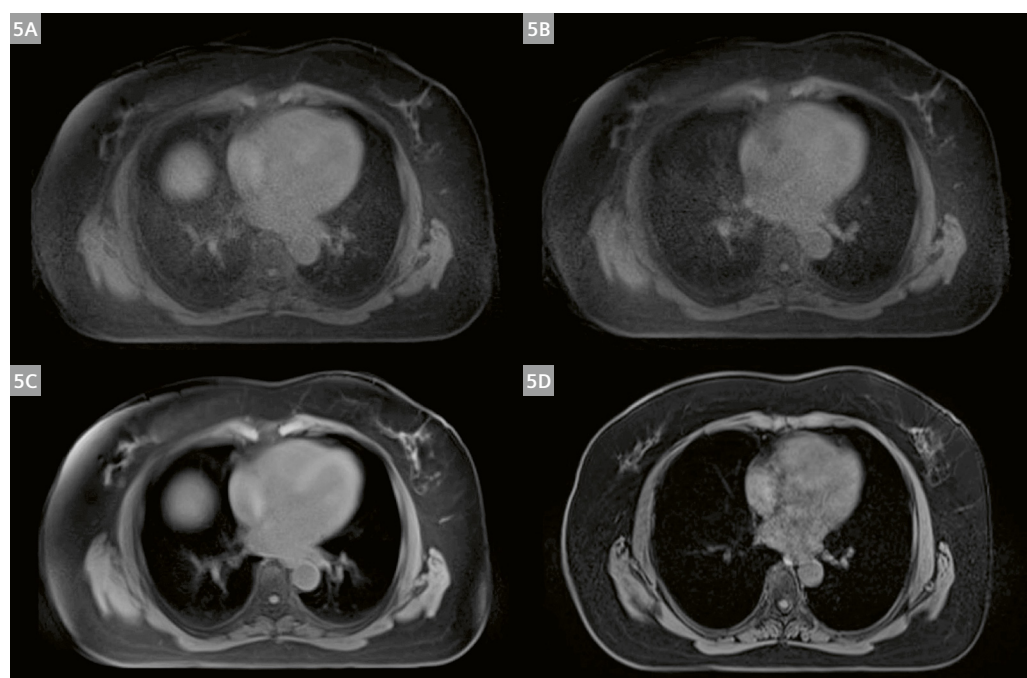
Discussion

The new breast MR-in-RT workflow in supine position allows breast and OAR depiction and motion evaluation with sharper images in end-of-exhale and a head-feet direction. We have shown that z-coverage comparable to CT examination is feasible in routine with different contrasts.

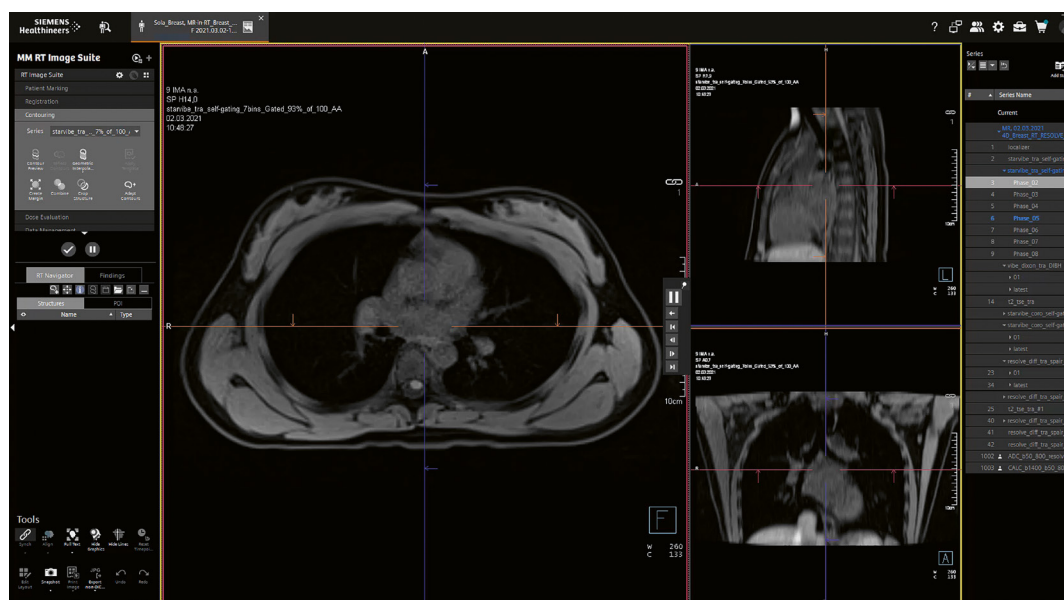
Our approach could fulfil the need for, e.g., partial breast irradiation, identification of marker clips, guidance for small cavities, and irradiation after tumor resection in

Median distance	FB end-of-exhale	FB end-of-inhale	DIBH
Heart–chest wall	2.4 ± 1.5 cm	3.0 ± 1.7 cm	4.0 ± 3.8 cm

Table 1: Median distance between heart and chest wall in different breathing states.



5 Axial views of the depicted breast and OAR in different breathing phases: (5A) 4D MRI Bin 1, end-of-exhale; (5B) 4D MRI Bin 7, end-of-inhale; (5C) 4D MRI average (sum of all radial views of 4D MRI); (5D) T1w VIBE Dixon in DIBH. Protocol can be set for up to 10 bins.



6 4D respiratory self-gating (4D MRI) image (Bin 1), RT Image Suite application.

free breathing. It could therefore optimize treatment for patients who cannot hold their breath. These patients might have difficulty holding their arms up after surgery, and MRI systems typically have smaller bore sizes than CT scanners. Nevertheless, the technique appears to be very promising for lymph node depiction in all contrasts and 4D MRI phases. The clear contouring of the heart (and OAR) in different phases would help reduce toxicity by minimizing dose during treatment.

By positioning the patient in the same way as with 4D CT or DIBH CT planning, the approach could potentially reduce registration errors. 4D MRI simplifies contouring compared to 2D cine imaging without comprising on covering the proper number of slices or volume. It would be interesting to evaluate margins in dose planning and the clinical evidence for less toxicity.

Conclusion

We have demonstrated the usefulness of 4D MRI with supine patient positioning in free breathing for treatment planning [7]. The same approach could eventually be extended to lung imaging at a lower field.

The new 4D workflow should play an important role in contouring and analyzing target and OAR motion to improve breast cancer treatment. Based on free-breathing techniques, future synthetic CT algorithms could be developed for the breast, lung, thorax, or abdomen regions for MR-only workflows.

Acknowledgments

We would like to thank Qfix & CIVCO Radiotherapy for providing us with the breast board.

References

- 1 World Health Organization, International Agency for Research on Cancer. Cancer Today. Accessed September 7, 2023. <https://gco.iarc.fr/today/home>.
- 2 Kirby AM, Evans PM, Donovan EM, Convery HM, Haviland JS, Yarnold JR. Prone versus supine positioning for whole and partial-breast radiotherapy: A comparison of non-target tissue dosimetry. *Radiother Oncol* 2010;96(2):178–84.
- 3 Grimm R, Block KT, Hutter J, Forman C, Hintze C, Kiefer B, et al. Self-gating reconstructions of motion and perfusion for free-breathing T1-weighted DCE MRI of the thorax using 3D stack-of-stars GRE imaging. In: Proceedings of the 20th scientific meeting, ISMRM, Melbourne, Australia. 2012; Abstract 598.
- 4 Henseler H, Ju X, Ray AK. Correlation of centroid-based breast size, surface-based breast volume, and asymmetry-score-based breast symmetry in three-dimensional breast shape analysis. *ISSN 2193–7052 GMS Ger Plast Reconstr Aesthet Surg*. 2016; 6: Doc03. <https://doi.org/10.3205/gpras000038>
- 5 Al-Ward SM, Kim A, McCann C, Ruschin M, Cheung P, Sahgal A, et al. The development of a 4D treatment planning methodology to simulate the tracking of central lung tumors in an MRI-linac. *J Appl Clin Med Phys*. 2018;19(1):145–155.
- 6 MR-integrated Workflows in Radiation Therapy (2018) published by Siemens Healthcare GmbH, Order No. A91MR-1100-95C-7600. Printed in Germany, 6085 04180.2. © Siemens Healthcare GmbH.
- 7 Habatsch M, Schneider M, Requardt M, Doussin S. Movement assessment of breast and organ-at-risks using free-breathing, self-gating 4D magnetic resonance imaging workflow for breast cancer radiation therapy. *Phys Imaging Radiat Oncol*. 2022;22:111–114.



Contact

Sylvain Doussin, Ph.D.
Siemens Healthineers
SHS DI MR R&D SWI AFT APPL
Allee am Roethelheimpark 2
91052 Erlangen
Germany
sylvain.doussin@siemens-healthineers.com

The Forgotten Effect of Radiation Therapy on Vessels and Circulating Blood

Felipe A. Calvo, M.D., Ph.D.^{1,2}; Rosa Meiriño, M.D., Ph.D.^{1,2}; Marina García-Cardosa³; Marta Vidorreta, Ph.D.⁴; Javier Burguete, Ph.D.³

¹Department of Radiation Oncology, Clínica Universidad de Navarra, Madrid, Spain

²Interdisciplinar Teragnosis and Radiosomics Research Group, Universidad de Navarra, Madrid, Spain

³Department of Physics and Applied Mathematics, Universidad de Navarra, Pamplona, Spain

⁴Siemens Healthineers, Madrid, Spain

Quality care in cancer treatment

Cancer is a curable disease. Its treatment typically requires a multidisciplinary approach, in which radiation therapy (RT) plays an important role. Between 50% and 70% of cancer patients receive RT as part of their treatment, and it contributes to curing the disease in more than 40% of cases [1].

Over the last decades, the evolution of RT has been tightly linked to technological development, which has enabled improved precision in dose-to-target radiation. Furthermore, personalized RT treatments have been facilitated by the use of treatment planning systems (TPSs) and a better understanding of the biological effects of the total dose administered. TPSs allow the integration of high-quality medical images (CT, MR, PET) and accurate mathematical algorithms for radiation dose distribution. As a result, virtual treatment planning is now a standard and fundamental requirement for high-quality cancer RT.

Despite this progress, several concepts deserve further investigation to improve cancer care. One of those is the impact of radiation exposure on vessels and circulating blood. Blood is a key biological component, and its exposure to radiation can have a direct effect on the patient's vascular health and immune defense (immunocompetence). Lymphocytes are the main line of defense against cancer, but they are unfortunately also extremely sensitive to even low doses of ionizing radiation [2]. Avoiding unnecessary irradiation of the patient's immune system is thus essential to improving clinical outcomes. Modern RT technology, including photon-, electron-, proton-, or heavy particle-based radiation beams, as well as more sophisticated TPSs that incorporate the dynamics of circulating blood in an individualized manner using 4D imaging techniques, will likely have a major impact on RT practice.

Our investigation focuses on studying the irradiated dose in vessels and circulating blood, developing algorithms for its estimation, evaluating its biological effect through circulating biomarkers, and comparing its impact on photon- and proton-based RT treatments. While both are high-precision techniques, proton therapy can provide more conformal radiation treatment, thus minimizing radiation dispersion into the surrounding tissues. The added exposure protection that proton-based therapy provides for vessels (and thus blood) could be key to improving long-term patient survival, as previous systematic studies have reported [3].

Dose-volume histograms and circulating blood

Dose-volume histograms (DVHs) are a mathematical representation of the cumulative dose distribution within a tissue volume. DVHs have become the main tool for graphically evaluating the dose received by both the oncological target and the surrounding tissue in RT treatment planning [4].

It was not until 2010 that DVHs of large vessels, such as the carotid artery, were included in irradiation plans. This was mainly due to the development of re-irradiation techniques [5]. The use of hypofractionated RT (in which the total radiation dose is divided into large doses, given over a shorter period than in conventional treatments) created the need for improved knowledge on the dose administered to these large vessels for estimating the potential long-term vascular toxicity in survivors [6]. However, to date, vascular structures are seldom delineated in the contouring process for dosimetric distribution assessment and are not evaluated in routine clinical practice during DVH analysis.

Some products/features mentioned herein are not commercially available in all countries and/or for all modalities. Their future availability cannot be guaranteed. Some are under development. Not available for sale.

Meanwhile, MR imaging has become very important in modern RT. This is due to its improved soft-tissue contrast and wide image design range, which allows in-depth characterization of both the tumor and its environment beyond what is possible with CT imaging. MRI-based flow techniques can provide a noninvasive, nonionizing method for accurate vascular assessment. The intrinsic sensitivity of MRI to motion offers the unique ability to acquire blood flow, while 3D spatial encoding offers the possibility of obtaining high spatial resolution images. Together, these features make it possible to visualize complex flow patterns in a 3D volume, along with the anatomical data.

Immune system and tumor response

Circulating blood is a biocellular complex that is equivalent to normal tissue at risk of radiation effects and has great relevance in oncology. The cellular components of blood (particularly lymphocytes, which are a type of white-blood or immune cell) are extremely radiosensitive, even to very low doses. Immunocompetence is highly affected by lymphopenia and even by induced subclinical damage to lymphocytes [3, 7–8]. All patients receiving RT have blood exposed to the effects of radiation, and 80% receive concomitant or sequential chemotherapy, further affecting their immune system.

Evidence of the immune system's contribution to radiation tumor response has increased in recent years. The systematic review published by Nessler et al. [9] summarizes the mechanisms identified to date that are involved in this response in a preclinical context, highlighting potential inflammatory and immune biomarkers of RT response. Some of these biomarkers are found within the tumor microenvironment, while others are circulating biomarkers that include different types of hematological cells, cytokines, and chemokines. Moreover, from a clinical point of view, there is strong, growing evidence of the prognostic impact of RT-induced lymphopenia as a factor associated with lower local control and patient survival in multiple cancer models [6, 7].

In clinical practice, existing biomarkers of vasculopathy and, more specifically, of endothelial injury, could be additionally monitored [10].

Abscopal effect

The abscopal effect (when untreated metastases respond to irradiation of a tumor elsewhere in the body) is a remarkable phenomenon in clinical radiobiology. It is mediated by the immune system activation against cancer cells, which results from the massive release of antigens in the irradiated region and the activation of systemic immunocompetence. Traditionally, this phenomenon has been known as an immunogenic activator (due to

the vaccine-like effect) of non-irradiated tumors or their systemic metastases [11, 12].

Some mechanisms of cell death, such as necrosis and necroptosis, can activate the immune system, triggering the proliferation of CD4+, CTL, and NK cells. When low radiation doses per fraction are used, the ratio of apoptosis to immune cell death is high. It seems that the conventional RT dose of 1.8–2 Gy is not sufficient to trigger immunogenic response. Interestingly, we can change this relationship and increase the mechanisms of immunological cell death, which include necrosis, necroptosis, and autophagy, by modifying the radiotherapy dose fractionation. Evidence from preclinical studies shows that doses greater than 8 Gy have strong effects on the immune responses of CTLs, CD4s, and NK cells. In this sense, irradiation techniques with qualitatively different dosimetric effects, such as photon therapy and proton therapy, may allow a proper evaluation of the effect of low-dose bath or dispersed doses on tissues involved on the irradiation plan [13].

Photons versus protons: Scatter radiation in clinical practice

The most advanced photon-beam techniques in high-precision RT (e.g., intensity-modulated RT and volumetric-modulated arc therapy) inevitably expose a significant volume of healthy anatomy to low-to-intermediate radiation. This includes vessels, circulating blood, and lymphatic structures. These levels of radiation have no value in terms of oncological benefit, and are therefore unnecessary and can be carcinogenic. In clinical practice, therefore, photon-beam RT is assumed to involve an iatrogenic element that can induce hematological damage [14, 15].

Conversely, proton therapy introduces dosimetric optimization with minimization of unnecessary dispersed dose, while maintaining high precision on the target (i.e., tumor, target volume, high-risk area). Moreover, proton-based therapy allows procedures to exclude large vessels and cardiac structures not requiring irradiation. Proton therapy can therefore be optimally combined with hypofractionated RT programs, as it allows to minimize irradiation re-exposure for circulating blood.

Our VASA research project

VASA stands for Vessels and Blood (“VASos” and “SAngrE”, in Spanish). Our primary goal is to study the relationship between the vascular, circulating irradiated volume and the radiobiological effects measured by biomarkers of endothelial damage, blood cytometry, and systemic immune outcome.

Our secondary goal is to generate an algorithm to implement patient-specific DVHs that take account of large

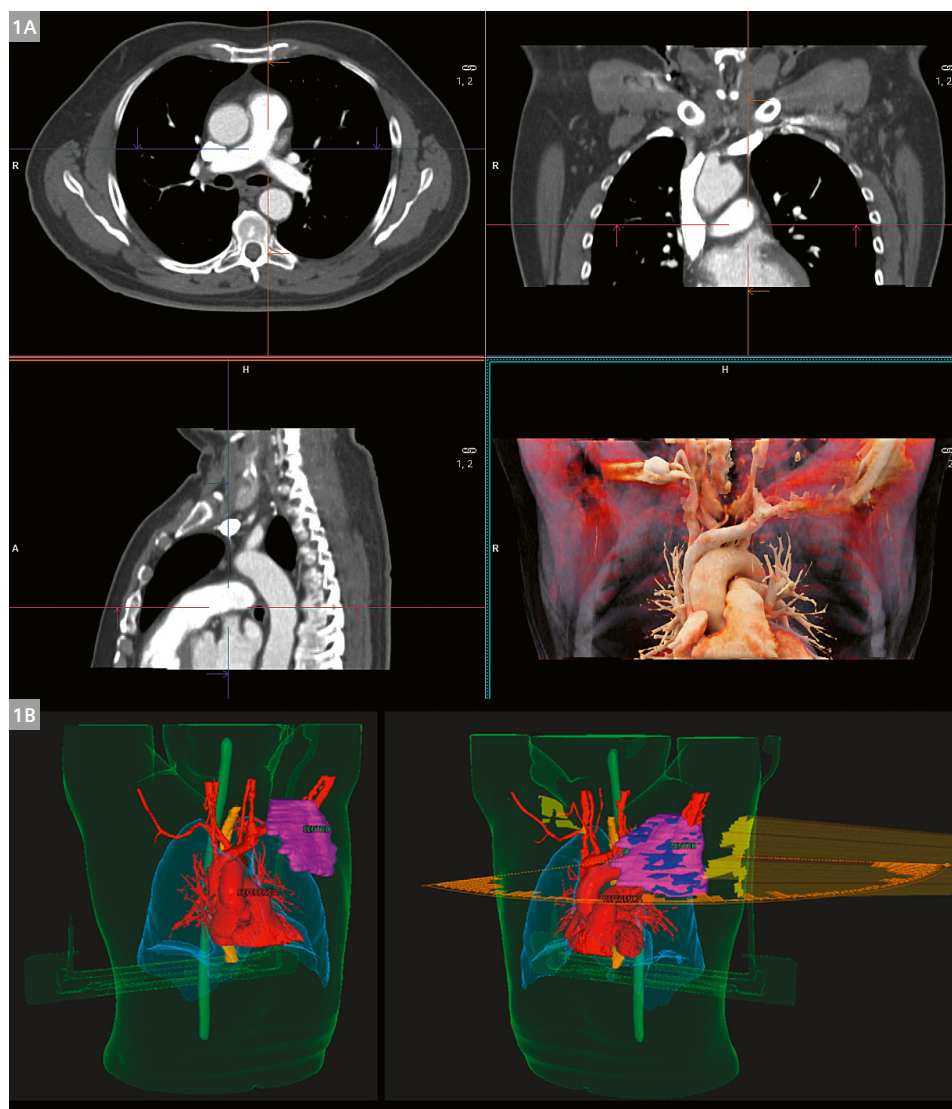
and medium vascular structures (arteries and veins) and circulating blood information measured from advanced imaging methods, as an element of potential dosimetric tests for personalized therapy.

We have divided the project into three phases:

- **Phase 1:** Feasibility in clinical practice of estimating DVHs of vascular structures using CT angiography (CTA) data and a Pinnacle treatment planning system (Philips, The Netherlands).
- **Phase 2:** Feasibility of combining the preliminary DVH data obtained in Phase 1 with MRI-based 3D flow information for circulating blood assessment, in conjunction with a dosimetric display generated in a RayStation treatment planning system (RaySearch Laboratories, Sweden), and the study of the dose

distribution relationship with the post-irradiation hematological effects, measured from serum biomarkers.

- **Phase 3 (in progress):** Systematic evaluation in clinical practice conditions of aggregating patient-specific vascular system, circulating blood, and DVHs in subject cohorts treated with the best available radiotherapy technique, including both photon and proton RT. A biological analysis of the irradiation effects caused by the dosimetric differences in the radiation exposure of different components of the immunosoma, by means of protecting vessels and circulating blood, as well as other organs of great immunological impact (such as intestinal microbiota, spleen, thymus, or liver), is being conducted in a prospective cohort with balanced representation of both photon and proton RT, according to the anatomico-vascular areas exposed to irradiation.



1 Photon RT treatment planning and CT-angiographic imaging overlay of a representative patient (RT target in thoracic region). Panel **(1A)** shows the maximum intensity projection (MIP) perfusion image derived from the CT perfusion acquisition, where blood vessel structures are clearly distinguishable from other tissues. Panel **(1B)** shows the vascular segmentation obtained with *syngo.via* from the CT MIP image (red), planning tumor volume (pink), and simulated isodoses (orange) over the planning CT image on the TPS.

Methods

Our study was conducted at the Madrid site of Clínica Universidad de Navarra, Spain. After giving informed consent, patients underwent a CT examination (SOMATOM Drive, VB20A, Siemens Healthcare, Forchheim, Germany) or, when indicated by their treatment planning, an MRI exam (3T MAGNETOM Vida, *syngo* MR XA20A, Siemens Healthcare, Erlangen, Germany). Blood samples were extracted at three time points (before, during, and at the end of treatment).

A 60-second dynamic perfusion scan was added to their routine CT examination, covering ~22 cm in the axial range, with 2 s and 1.5 mm temporal and slice resolution, respectively. An additional 1 mm resolution acquisition was added 75 s after, with wide range coverage. Data were processed in *syngo.via* (VB50, Siemens Healthcare, Forchheim, Germany) using CT Body Perfusion and MM Reading tools, to extract vessel masks. Segmentation was performed by a trained oncologist, and results were overlayed on the patient's DVH in the TPS, to estimate the dose irradiated to the vessel regions (Fig. 1).

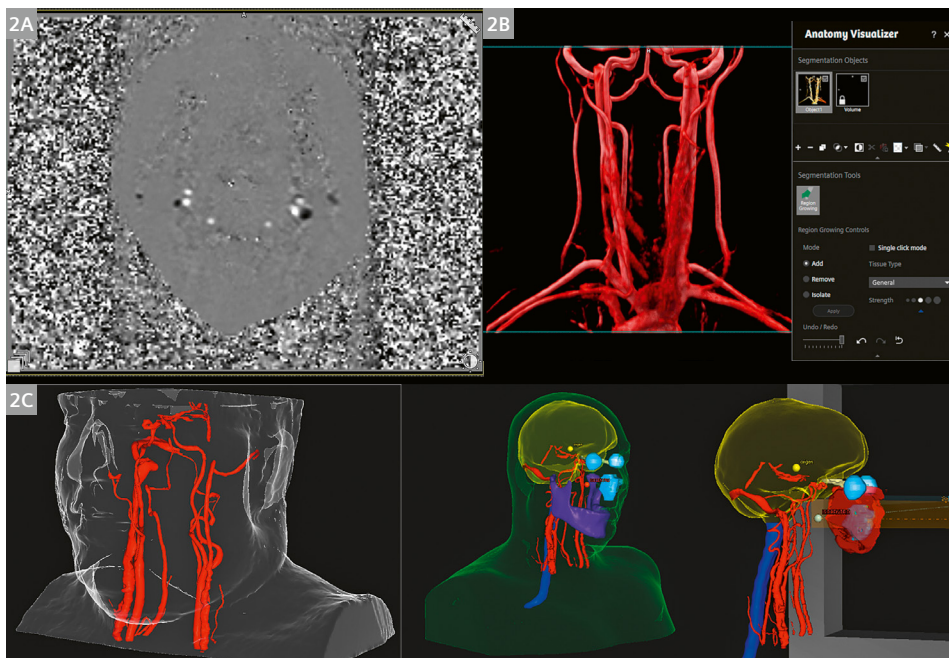
Similarly, two 3D phase-contrast flow MRI sequences were added to the prescribed MR examination, each one with 3 separate velocity encoding (VENC) directions to cover all spatial dimensions, and a volume coverage of ~22 cm in the z-direction. The VENC was adjusted for each measurement to optimize velocity imaging in arteries and veins, according to the anatomical region of interest. For instance, in the neck, default VENCs were adjusted to 50 and 20 cm/s, while in the abdomen, higher VENCs were

selected to adjust for faster flow in the descending aorta and inferior cava vein. Image resolution was adjusted to the vessel size of the target region: 1 mm for head scans and 1.7 mm for body scans. In thoracic and abdominal regions, respiratory navigation was employed to minimize motion artifacts caused by breathing. The navigator strategy included in this sequence (ReCAR) provides smart *k*-space ordering based on the detected respiratory position, thus leading to increased navigator acceptance rates. The total added scan time of these two measurements was 10–20 min, depending on the target area, the use of navigator, and the subject's breathing rate.

The magnitude sum (MSUM) image, reconstructed from the magnitude images of all three flow encoding directions, was used to segment the vessels and create a vessel mask. Segmentation was also performed in *syngo.via* by a trained oncologist and exported to the TPS for final CT-MR registration. The phase (P) images were processed to correct potential aliasing and 3D velocity fields were derived in MATLAB (MathWorks, Natick, MA, USA), in collaboration with the Physics and Applied Mathematics Department of the University of Navarra (Figs. 2, 3).

Preliminary results

We found a link between lymphopenia patterns and the arterial vessel volume exposed to irradiation [16]. Lymphocyte count is considered a biomarker of the dose delivered to this biological target. In *N* = 20 patients treated with photon RT, DVHs were generated to estimate the correlation between dosimetric value and lymphocyte count



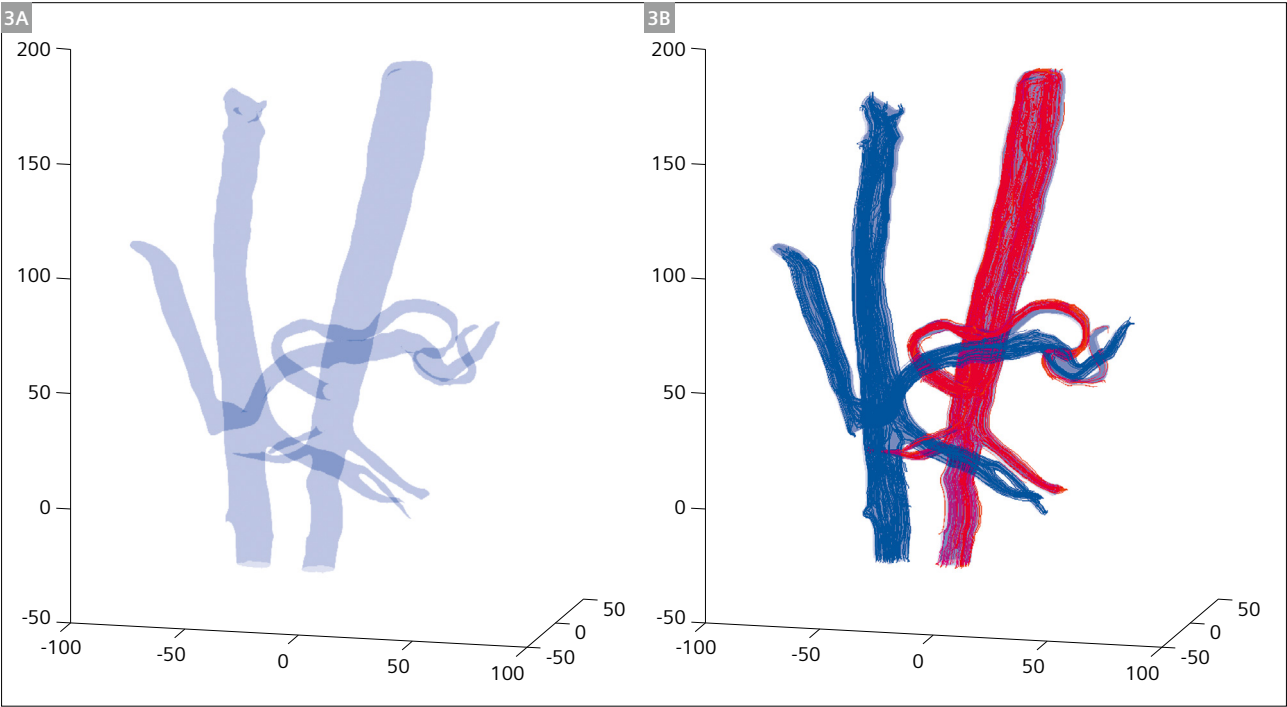
2 MRI-based 3D flow acquisition and vessel segmentation results on a representative subject (RT target in neck region). **(2A)** Phase map showing velocity encoding in slice direction, depicting artery and venous signal in white and black, respectively; **(2B)** volume rendering of the magnitude sum (MSUM) image, from which vessel segmentation is performed in *syngo.via* using tools like Region Growing; and **(2C)** final segmentation and target volume dose overlay in TPS.

(Table 1), finding that an effective dose to immune cells (EDIC) of 4 Gy showed significant more grade 3–4 lymphopenia than those with EDIC < 4 Gy. This same trend was observed in relation to the integral dose (ID) in vessels greater than 1 Gy*L.

While CTA imaging allows high-resolution visualization and segmentation of the vascular tree, MRI’s intrinsic sensitivity to movement offers the unique ability to acquire blood flow simultaneously with the anatomical data within a single measurement. It also makes it possible to implement vascular segmentation without subjecting the patient to greater exposure to radiation and in a reasonable time. In particular, 3D phase-contrast flow MRI methods allow the volumetric acquisition of blood dynamics, including blood velocity and flow, without the need to

expose the patient to added scan radiation and the administration of iodinated contrast. Furthermore, by adjusting the VENC, it allows the study of both arterial and venous blood patterns (Fig. 2). We investigated the potential of 3D MR-based flow imaging to provide vascular segmentation in a reasonable time in the context of treatment planning [17, 18]. Our findings corroborate the feasibility of using MRI flow, with similar overall added protocol acquisition time, while achieving superior venous visualization due to the adaptation flexibility of the VENC parameter.

We then introduced the MR flow segmentation into the dosimetric treatment planning (Fig. 4) to estimate the exposure of circulating blood to irradiation in a cohort of N = 30 patients treated by either photon RT or proton RT [19]. A significant difference in EDIC was found in patients



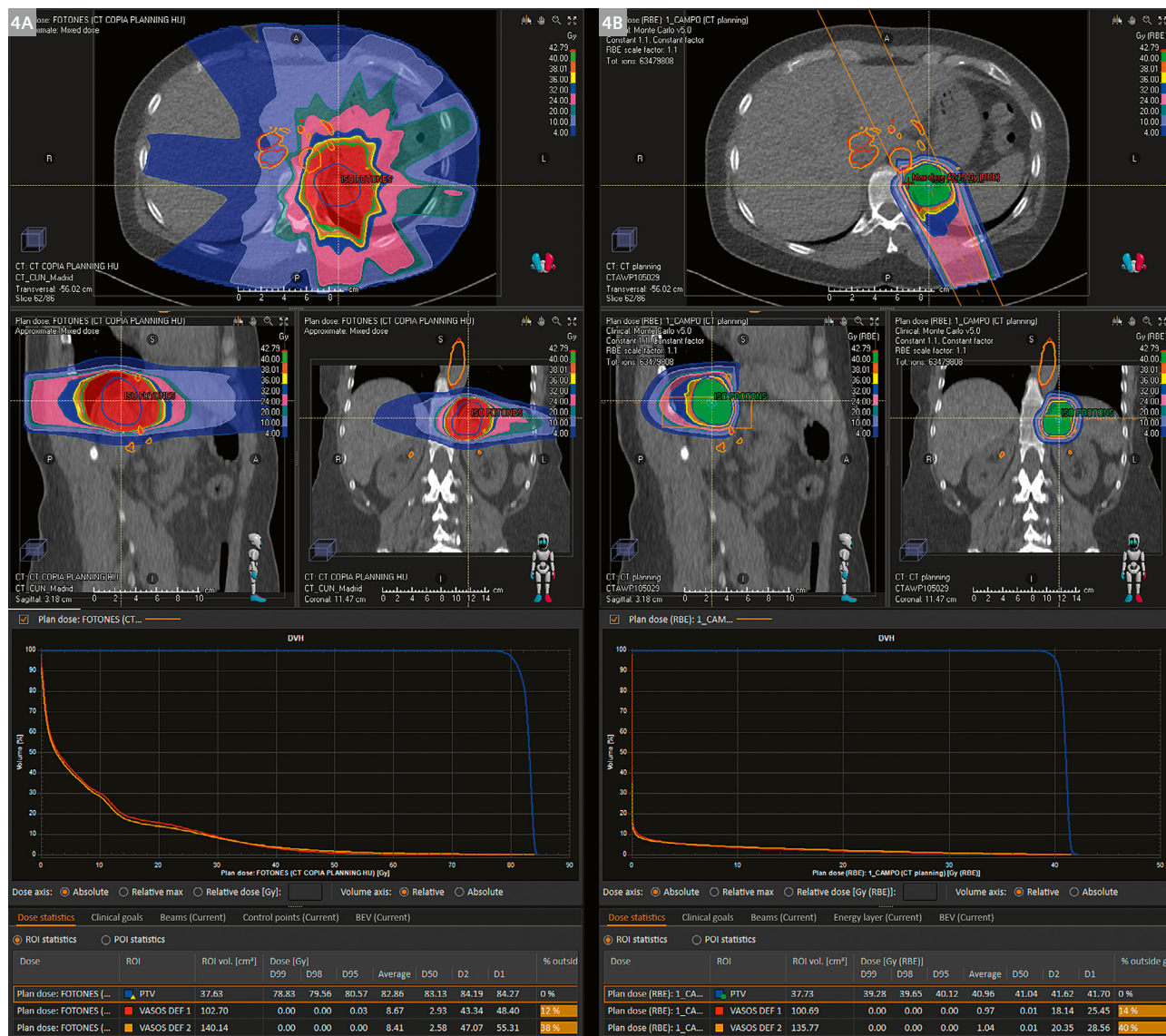
3 Example of (3A) vessels mask and (3B) velocity field trajectories, derived from the 3D MRI velocity-encoded phase images. These data were generated in collaboration with the Physics and Applied Mathematics Department of the University of Navarra using MATLAB (MathWorks, Natwick, MA, USA). The acquisition shows both the abdominal aorta (red) and inferior vena cava (blue) sections.

Total effective dose to immune cells (EDIC) [Gy]	Bone integral dose (DI) [Gy*L]	Vessels integral dose (DI) [Gy*L]	No Lymphopenia	Lymphopenia grade I-II	Lymphopenia grade III-IV
6.5 [2–16.5]	17.8	1.8	6 (30%)	7 (35%)	7 (35%)

Table 1: Hematological (immunity) assessment and mean vessel dose distribution on N = 20 patients treated with photon-based RT, studied with CT-angiographic imaging. A total of 60% and 40% of supra- and infra-diaphragmatic regions were irradiated, respectively. Patients received a mean of 21 fractions [range = 14–33] during treatment. Mean planned target and vascular volumes were 745 and 149 cc, respectively, as derived from the segmentations.

treated by photon RT compared to proton RT (4.11 vs. 1.25 Gy). Similarly, the mean ID in vessels was significantly higher in photon RT than in proton RT (4.9 vs. 0.38 Gy*L)

(Table 2). Additionally, preliminary correlations with lymphopenia patterns were observed after both proton and photon irradiation.



4 Photon (4A) vs. proton (4B) therapy treatment planning and MRI-flow overlay for a representative patient (RT target in abdominal target region). The calculated average vessel dose in vessels is 8.67 Gy and 0.97 Gy, respectively. The planning target volume (PTV) region contour is highlighted in blue, while vessel contours are shown in red and orange.

	Total effective dose to immune cells (EDIC) [Gy]	Vessels integral dose (DI) [Gy*L]	Initial lymphocyte count [10 ⁹ /L]	Mid-treatment lymphocyte count [10 ⁹ /L]	Final lymphocyte count [10 ⁹ /L]
Photon RT	5.18	4.92	1.50	0.86	0.65
Proton RT	1.33	0.40	1.95	1.66	1.41

Table 2: Hematological (immunity) assessment and mean vessel dose distribution on N = 30 patients assigned to either photon- or proton-based RT treatment, studied with MRI 3D flow imaging. A total of 73% and 27% of supra- and infra-diaphragmatic regions were irradiated, respectively. Mean planned target and vascular volumes were 382 and 495 cc, respectively, as derived from the segmentations. Note that now both, arterial and venous vessels are included in the analysis.

Potential medical benefits

A systematic study of the radiation impact on vessels and circulating blood could bring a paradigm shift in clinical radiotherapy practice, facilitating

- new dosimetric strategies in daily practice to exclude these areas from unnecessary irradiation;
- prediction of hematological toxicity (relevant for adjusting the intensity of chemotherapy administration);
- prediction of the immunocompetence status (important when considering immunotherapy agents);
- long-term vascular risk predictions;
- prediction of the potential abscopal effect linked to irradiation (i.e., promotion of systemic antitumor effect with focal radiotherapy);
- establishment of a multifactorial personalized immune-dosimetric nomogram integrating objective biomarker measurements.

In summary, this could open up new opportunities for further optimization of RT planning, with significant clinical dosimetric advantages (e.g., immunocompetence, prevention of vascular and inflammatory intestinal diseases). The added knowledge could help further promote the preservation of immunocompetence by modifying RT techniques toward less lymphopenic strategies (e.g., hypofractionated radiation, FLASH delivery [20], high precision adaptive RT), to minimize unnecessary irradiation of anatomical areas with low-to-intermediate doses.

Acknowledgments

We thank Dr. Ning Jin and Dr. Daniel Giese from the MR predevelopment team for supporting this project with the Advanced Flow Imaging WIP. We also thank Siemens Healthineers Spain for their continuous support of this research.

References

- 1 Baskar R, Lee KA, Yeo R, Yeoh KW. Cancer and radiation therapy: Current advances and future directions. *Int J Med Sci* 2012;9(3):193-199.
- 2 Braeman J. Lymphocyte response after radiotherapy. *Lancet* 1973;2(7830):683.

Contact

Felipe A. Calvo, M.D., Ph.D.
Codirector of the Radiation Oncology
Department & Scientific Director
of the Proton Therapy Unit
Clínica Universidad de Navarra
Marquesado de Santa Marta, 1
28027 Madrid
Spain
Tel.: +34 91 3531920
fcalvom@unav.es



- 3 Venkatesulu BP, Mallick S, Lin SH, Krishnan S. A systematic review of the influence of radiation-induced lymphopenia on survival outcomes in solid tumors. *Crit Rev Oncol Hematol*. 2018;123:42-51.
- 4 Lyman JT. Complication probability as assessed from dose-volume histograms. *Radiat Res Suppl* 1985;8:S13-19.
- 5 Rosenthal DI, Fuller CD, Barker JL Jr, Mason B, Garcia JA, Lewin JS, et al. Simple carotid-sparing intensity-modulated radiotherapy technique and preliminary experience for T1-2 glottic cancer. *Int J Radiat Oncol Biol Phys*. 2010;77(2):455-461.
- 6 Xue J, Kubicek G, Patel A, Goldsmith B, Asbell SO, LaCouture TA. Validity of Current Stereotactic Body Radiation Therapy Dose Constraints for Aorta and Major Vessels. *Semin Radiat Oncol*. 2016;26(2):135-139.
- 7 Upadhyay R, Venkatesulu BP, Giridhar P, Kim BK, Sharma A, Elghazawy H, et al. Risk and impact of radiation related lymphopenia in lung cancer: A systematic review and meta-analysis. *Radiother Oncol*. 2021;157:225-233.
- 8 Heylmann D, Ponath V, Kindler T, Kaina B. Comparison of DNA repair and radiosensitivity of different blood cell populations. *Sci Rep*. 2021;11(1):2478.
- 9 Nessler JP, Schaeue D, McBride WH, Nickers P. Biomarqueurs inflammatoires et immunologiques de réponse à la radiothérapie [Inflammatory and immune biomarkers of radiation response]. *Cancer Radiother*. 2018;22(2):180-192. French.
- 10 Venkatesulu BP, Mahadevan LS, Aliru ML, Yang X, Bodd MH, Singh PK, et al. Radiation-Induced Endothelial Vascular Injury: A Review of Possible Mechanisms. *JACC Basic Transl Sci*. 2018;3(4):563-572.
- 11 Rodriguez-Ruiz ME, Rodriguez I, Leaman O, López-Campos F, Montero A, Conde AJ, et al. Immune mechanisms mediating abscopal effects in radioimmunotherapy. *Pharmacol Ther*. 2019;196:195-203.
- 12 Rodríguez-Ruiz ME, Rodríguez I, Mayorga L, Labiano T, Barbes B, Etcheberria I, et al. TGFβ Blockade Enhances Radiotherapy Abscopal Efficacy Effects in Combination with Anti-PD1 and Anti-CD137 Immunostimulatory Monoclonal Antibodies. *Mol Cancer Ther*. 2019;18(3):621-631.
- 13 Demaria S, Formenti SC. The abscopal effect 67 years later: from a side story to center stage. *Br J Radiol* 2020;93(1109):20200042.
- 14 Mohan R, Liu AY, Brown PD, Mahajan A, Dinh J, Chung C, et al. Proton therapy reduces the likelihood of high-grade radiation-induced lymphopenia in glioblastoma patients: phase II randomized study of protons vs photons. *Neuro Oncol*. 2021;23(2):284-294.
- 15 Zou Z, Bowen SR, Thomas HMT, Sasidharan BK, Rengan R, Zeng J. Scanning Beam Proton Therapy versus Photon IMRT for Stage III Lung Cancer: Comparison of Dosimetry, Toxicity, and Outcomes. *Adv Radiat Oncol*. 2020;5(3):434-443.
- 16 Meiriño RM, Calvo FA, Aguilar B, Azcona JD, Burguete J, Pascau J, et al. Patterns of lymphopenia and dose to circulating blood estimated by angio-TAC: prospective pilot study in standard clinical practice. *Clin Transl Oncol* 2021;24:1-163.
- 17 Meiriño RM, Calvo FA, Serrano J, Aristu JJ, Palma J, Cambeiro M, et al. Vascular assessment for radiotherapy planning: prospective study with 4d-MRI-flow. *Clin Transl Oncol*. 2022;24(Extraord. 1):163.
- 18 Meiriño RM, Calvo FA, Burguete J, Serrano-Andreu J, Aristu J, Azcona D, et al. PO-1885 Analysis of Vascular and Circular Blood in Radiation Treatment Planning: Technological Options. *Radiother Oncol* 2022;170 Suppl 1:S1670-1671. [https://www.thegreenjournal.com/article/S0167-8140\(22\)03848-8/pdf](https://www.thegreenjournal.com/article/S0167-8140(22)03848-8/pdf)
- 19 Meiriño RM, Calvo FA, et al. Lymphopenia Patterns and Radiation Dose in Circulating Blood Estimated by Magnetic Resonance Imaging (MRI) Flow. *PTCOG-61*, 2023.
- 20 Cucinotta DA, Smirnova OA. Effects of Flash Radiotherapy on Blood Lymphocytes in Humans and Small Laboratory Animals. *Radiat Res* 2023;199(3):240-251.

Bring-Your-Own-Phantom (BYOP): A Flexible Stand-Alone Distortion Analysis Prototype

Lumeng Cui, Ph.D.¹; Gerald Moran, Ph.D.²; Niranjan Venugopal, M.Sc., Ph.D., MCCPM^{3,4,5}

¹Research Scientist, Siemens Healthcare Limited, Oakville, Ontario, Canada

²Director of Research, Siemens Healthcare Limited, Oakville, Ontario, Canada

³Department of Medical Physics, CancerCare Manitoba, Winnipeg, Manitoba, Canada

⁴Department of Physics and Astronomy, University of Manitoba, Winnipeg, Manitoba, Canada

⁵Department of Radiology, University of Manitoba, Winnipeg, Manitoba, Canada

Short synopsis

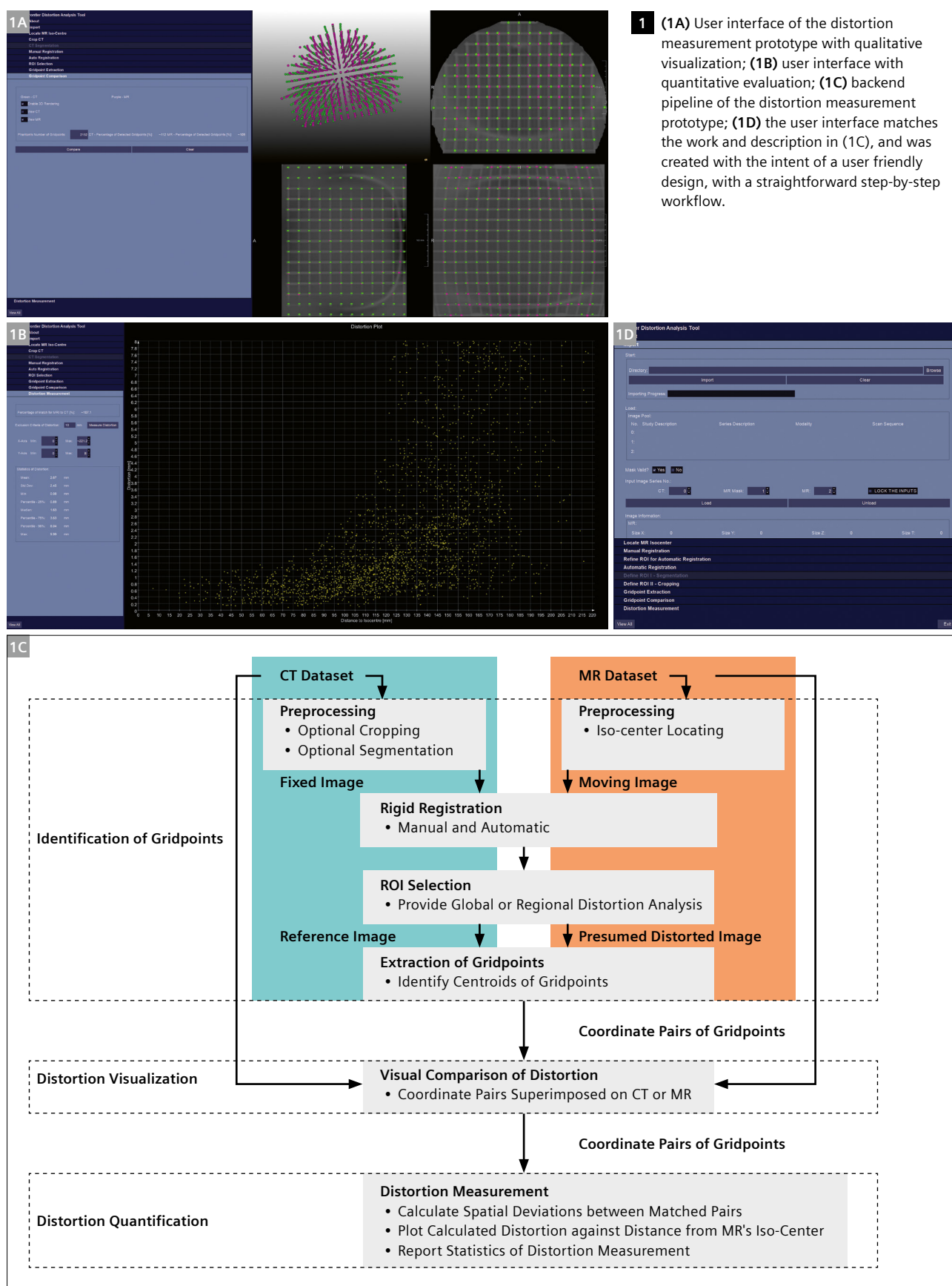
Magnetic Resonance Imaging (MRI) is increasingly becoming an essential component in radiation therapy (RT) planning and with it, characterization of the geometric distortion latent in MR imaging. Current methods available for performing distortion measurements are often performed as offline calculations. In this work, we have developed a prototype that can accommodate any type of grid-like phantom and provides an on-the-scanner software solution for the analysis of spatial distortion MR images. The prototype takes a prior CT scan and a newly acquired MR dataset as inputs and generates a qualitative visualization and quantitative evaluation for the spatial distortion in the MRI volume. The prototype was assessed using three grid-like phantoms with good success.

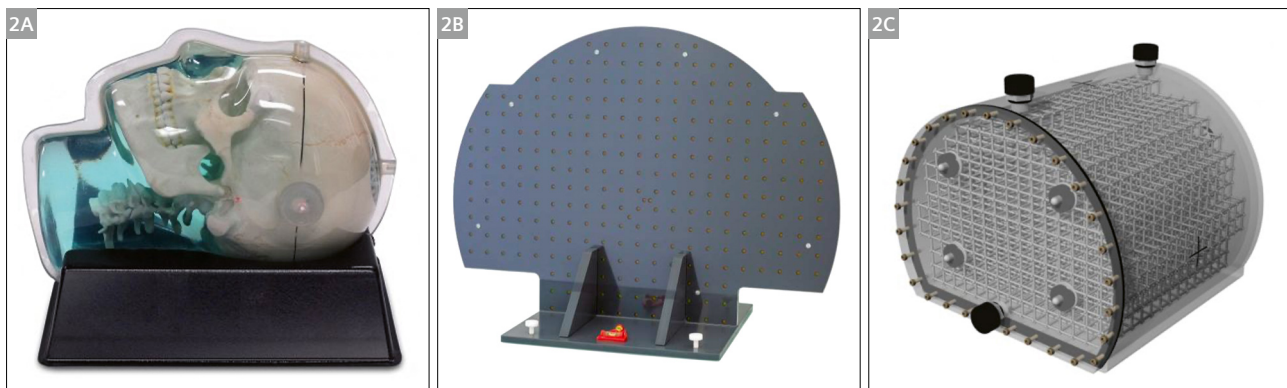
Introduction

The characterization of distortion in MRI is not a new phenomenon. In fact, our understanding of the topic goes back almost 30 years, when MRI was being used for stereotactic radiation therapy [1–5]. In that era of radiation treatment planning, the MR image was often fused to the computed tomography (CT) image via image registration. Since the images were co-registered, the MR image was primarily used to delineate the cancer, which could not be seen on the CT image. In this scenario, the spatial fidelity of the MRI was of less importance since the CT image was the primary dataset being used to position the patient and perform the necessary dose calculations. Fast-forward 30 years, and the use of MRI for radiotherapy remains very much the same at many centers, with the MRI being used for delineation via image registration. But a lot has changed in three decades: Radiation oncology has trended toward treatments that are depositing much more radiation dose in far fewer fractions. In this new paradigm, the precision and accuracy of radiation treatments have increased. The drive for more precision targeting has led to the development of MR-only radiation treatment workflows, and systems that combine MRI and linear acceleration, known as MR-Linacs [6–8]. Because of this trend,

we have seen increased attention being paid to methods of spatial distortion correction and to various ways of characterizing the residual distortion [9–13]. A lot of work has been done to understand the effect of MRI distortion for specific treatment sites [14–20].

Thus, MRI is increasingly being used in radiation therapy procedures, and measuring residual geometric distortion has become even more vital. Even though MRI can provide superior soft-tissue contrast than CT imaging, MRI suffers spatial distortion deviating from isocenter due to the nonlinearity of magnetic gradients. This spatial distortion increases with increasing distance from the isocenter. Although vendor-supplied correction algorithms can help mitigate the spatial distortion, there is still a need to monitor any potential distortion that might jeopardize the safety and accuracy of the MR imaging that is being incorporated into radiation treatment planning. In this regard, proper software and (grid-like) phantoms are indispensable for performing an accurate distortion measurement and quality-control monitoring. However, in the current marketplace, phantoms and software used for distortion measurements are often expensive and require subscriptions for software, which may hinder smaller





2 (2A) Anthropomorphic skull phantom with a grid spacing of 15 mm and grid diameter of 3 mm (Model 603A, CIRS Inc.); (2B) generic large-field 2D phantom with a grid spacing of 30 mm and grid diameter of 5 mm (Siemens Healthcare); and (2C) generic large-bore 3D phantom with a grid spacing of 20 mm and grid diameter of 3 mm (Model 604, CIRS Inc.).

centres with limited resources. Most of the current software also requires the user to perform this type of analysis offline. Because of these limitations, we sought to provide a flexible solution where the user can bring their own “grid-like” phantoms (which could be 3D-printed in-house) and perform the analysis directly on the scanner, within the software ecosystem of the console. In this work, we developed a novel online distortion measurement prototype that can either be housed in the scanner’s ecosystem, allowing an “on-the-fly” distortion assessment on the MR console, or operate offline on a personal computer (PC) for standalone analysis.

Methods

The distortion measurement prototype was developed on the *syngo.via* Frontier platform (Siemens Healthcare, Erlangen, Germany). It can be integrated into the inline *syngo.via* MRI ecosystem from Siemens Healthcare, or it can operate offline as standalone software available on a Windows® system. The prototype requires a CT image of the phantom as a reference image. Acquired MR images are compared against the reference, and the software computes the distortion as a function of distance from isocentre. The prototype’s user interface and backend processing pipeline are described in Figure 1, and the methods for extracting grid points are based on the approaches proposed by Stanescu et al. [21]. Three different types of distortion phantoms containing orthogonal grids of rods were used in this study to demonstrate the efficacy and versatility of the prototype. As shown in Figure 2, these phantoms include an anthropomorphic skull phantom (Model 603A, CIRS Inc., Norfolk, VA, USA), a generic large-field 2D phantom (Siemens Healthcare; note that LAP have a commercialized THETIS phantom developed on the basis of the prototype 2D phantom from Siemens Healthcare),

and a generic large-bore 3D phantom (Model 604, CIRS Inc., Norfolk, VA, USA). To summarize the distortion, the prototype uses the extracted grid points from both CT and MR to provide not only an intuitive visual comparison but also a quantitative evaluation, including their calculated distortion deviations against the distance to isocenter with statistical information (i.e., minimum, maximum, and mean residual distortion). Lastly, the results can be saved locally by exporting the displayed data as a comma-separated values (CSV) file. The export file contains both scanner-specific information (field strength, gradient type, scanner make, etc.) and coordinates from the MR and CT datasets used for statistical analysis, which could be imported into quality assurance tracking programs.

Results

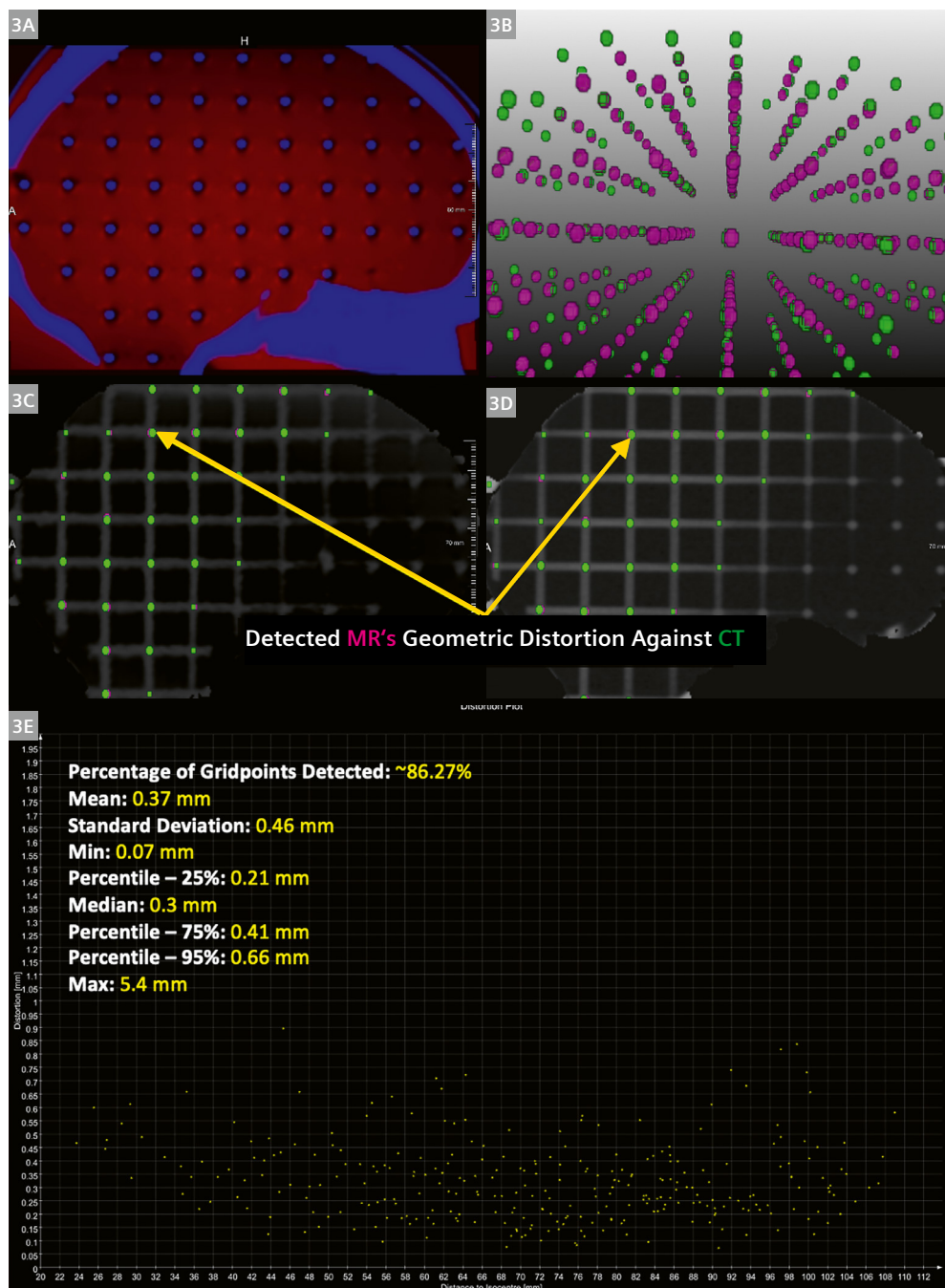
Figures 3, 4, and 5 show the distortion assessments produced by the prototype for, respectively, the CIRS skull phantom, the 2D large-field phantom from Siemens Healthcare, and the CIRS large-bore phantom. Panel A in each of the figures shows the results of the automatic rigid image registration displayed at the slice near the isocenter. The CT (blue) and MRI (red) datasets are well matched. Panel B in each figure is the 3D rendering of the representations of the grid points’ coordinate pairs (MRI: magenta, CT: green), providing an overall visualization of the spatial distortion for users. Panels C and D display the calculated coordinates positioned at the center of the grid points of the MR and CT images. Panels C and D also exhibit the qualitative spatial distortion between the acquired MR image compared to the reference CT image. Panel E summarizes a quantitative evaluation of the distortion measurement from MR for each phantom, including a distortion plot and statistical information.

Discussion

The software prototype¹ requires, at a minimum, a reference CT image and a single MR image. By design, the software can analyze most types of grid-like phantoms, as demonstrated in this work. This allows users to 3D-print their own phantom for custom use cases. The rigid image

registration is the first step to ensure the accuracy of distortion measurements since a potential inaccuracy in co-registration between two modalities will bring additional spatial deviations. In the prototype, we perform a manual registration followed by an auto-registration step to minimize the spatial discrepancy. Otherwise, the auto-registration might prioritize the minimization of the spatial variation resulting from the geometric distortion.

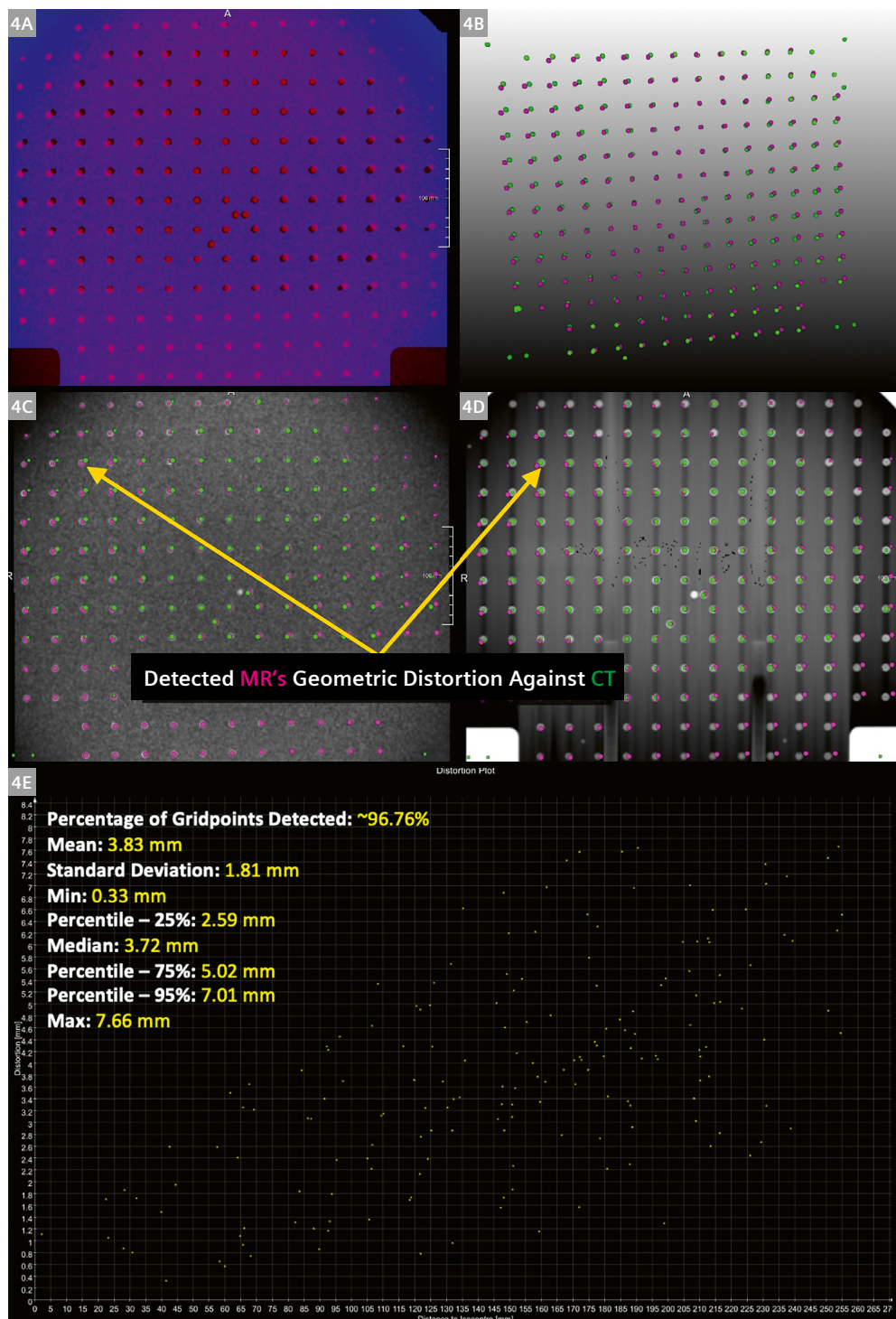
¹Work in progress. The application is currently under development and is not for sale in the U.S. and in other countries. Its future availability cannot be ensured.



3 Using the CIRS 603A, we present **(3A)** the results of rigid registration displayed at the slice near the isocenter (MR: red, CT: blue); **(3B)** 3D rendering of the representations of the grid points' coordinate pairs (MR: magenta, CT: green); **(3C)** coordinate pairs superimposed on MR image; **(3D)** coordinate pairs superimposed on CT image; and **(3E)** distortion plot against the distance from the isocenter.

Once the proper registration is visually verified, the extraction method can effectively detect the grid points for either MR (Figs. 3–5C) or CT (Figs. 3–5D) in each phantom, despite differences in contrast between MR and CT. The distortion can then be inspected slice by slice in an orthogonal view or a perspective 3D view. Sometimes,

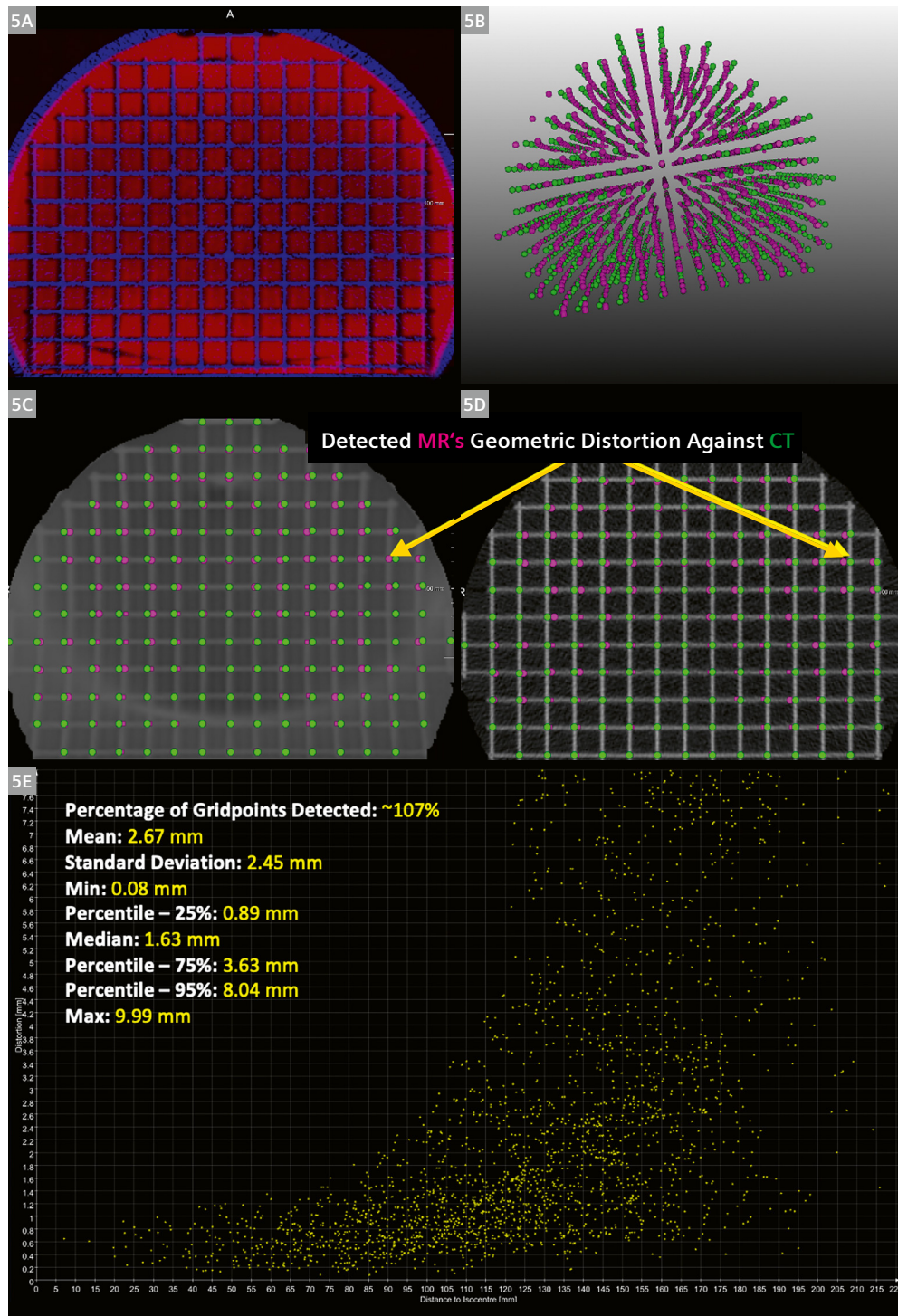
the points might be misidentified due to imaging artifacts. This issue can be easily addressed by acquiring CT and MR images with more homogenous intensity, finer contrast, and higher resolution. Lastly, for the distortion plot, the 2D large-field phantom and the 3D large-bore phantom suggest a trend of increasing spatial distortion



- 4** Using the 2D large-field phantom from Siemens Healthcare, we present **(4A)** the results of rigid registration displayed at the slice near the isocenter (MR: red, CT: blue); **(4B)** 3D rendering of the representations of the grid points' coordinate pairs (MR: magenta, CT: green); **(4C)** coordinate pairs superimposed on MR image; **(4D)** coordinate pairs superimposed on CT image; and **(4E)** distortion plot against the distance from the isocenter.

with increasing distance from the isocenter, which corresponds to our expectations. On the other hand, the skull phantom did not show a similar upward trend because of the smaller field of view. In summary, achieving accurate spatial distortion measurements using our prototype relies on high-quality images, which can be achieved using optimized CT and MR protocols.

Please note that THETIS 3D MR Distortion Phantom test protocols are available on the MAGNETOM World Website in order to run QA tests: <https://www.magnetomworld.siemens-healthineers.com/clinical-corner/protocols/mr-in-rt/thetis-3d-mr-distortion-phantom-test>



- 5 Using the CIRS large-bore phantom, we present (5A) the results of rigid registration displayed at the slice near the isocenter (MR: red, CT: blue); (5B) 3D rendering of the representations of the grid points' coordinate pairs (MR: magenta, CT: green); (5C) coordinate pairs superimposed on MR image; (5D) coordinate pairs superimposed on CT image; and (5E) distortion plot against the distance from the isocenter.

Conclusion

This work develops a novel online software prototype which can provide automatic vivid visualization and quantitative evaluation of spatial distortion for both small and large grid-like phantoms.

Summary of main findings

The novelty of this work is the software prototype¹, which may be used as a standalone solution or run directly on the MR console. It can also be incorporated into the MR ecosystem, thus providing an online solution that users can easily access for routine quality assurance of MR images for radiation treatment planning.

¹Work in progress. The application is currently under development and is not for sale in the U.S. and in other countries. Its future availability cannot be ensured.

References

- Schad LR, Ehrlicke HH, Wowra B, Layer G, Engenhart R, Kauczor HU, et al. Correction of spatial distortion in magnetic resonance angiography for radiosurgical treatment planning of cerebral arteriovenous malformations. *Magn Reson Imaging*. 1992;10(4):609–621.
- Maurer CR Jr, Aboutanos GB, Dawant BM, Gadamssetty S, Margolin RA, Maciunas RJ, et al. Effect of geometrical distortion correction in MR on image registration accuracy. *J Comput Assist Tomogr*. 1996;20(4):666–679.
- Moerland MA, Beersma R, Bhagwandien R, Wijrdeman HK, Bakker CJ. Analysis and correction of geometric distortions in 1.5 T magnetic resonance images for use in radiotherapy treatment planning. *Phys Med Biol*. 1995;40(10):1651–1654.
- Kooy HM, van Herk M, Barnes PD, Alexander E 3rd, Dunbar SF, Tarbell NJ, et al. Image fusion for stereotactic radiotherapy and radiosurgery treatment planning. *Int J Radiat Oncol Biol Phys*. 1994;28(5):1229–1234.
- Chomy F, Muyldermans P, Chemin A, Kind M, Thomas L, Le Treut AL, et al. [MRI and radiotherapy. External references, selection of plans and measurement of distortion]. *Bull Cancer Radiother*. 1994;81(3):241–246. French.
- Hall WA, Paulson ES, van der Heide UA, Fuller CD, Raaymakers BW, Legendijk JJW, et al. The transformation of radiation oncology using real-time magnetic resonance guidance: A review. *Eur J Cancer*. 2019;122:42–52.
- Das JJ, McGee KP, Tyagi N, Wang H. Role and future of MRI in radiation oncology. *Br J Radiol*. 2019;92(1094):20180505.
- Legendijk JJ, Raaymakers BW, van Vulpen M. The magnetic resonance imaging-linac system. *Semin Radiat Oncol*. 2014 Jul;24(3):207–209.
- Gao Y, Yoon S, Savjani R, Pham J, Kalbasi A, Raldow A, et al. Comparison and evaluation of distortion correction techniques on an MR-guided radiotherapy system. *Med Phys*. 2021;48(2):691–702.
- Tadic T, Jaffray DA, Stnescu T. Harmonic analysis for the characterization and correction of geometric distortion in MRI. *Med Phys*. 2014;41(11):112303.
- Wachowicz K, Stnescu T, Thomas SD, Fallone BG. Implications of tissue magnetic susceptibility-related distortion on the rotating magnet in an MR-linac design. *Med Phys*. 2010 Apr;37(4):1714–1721.
- Crijns SP, Raaymakers BW, Legendijk JJ. Real-time correction of magnetic field inhomogeneity-induced image distortions for MRI-guided conventional and proton radiotherapy. *Phys Med Biol*. 2011;56(1):289–297. Epub 2010 Dec 9.
- Baldwin LN, Wachowicz K, Thomas SD, Rivest R, Fallone BG. Characterization, prediction, and correction of geometric distortion in 3 T MR images. *Med Phys*. 2007;34(2):388–399.
- Sullivan TP, Harkenrider MM, Surucu M, Wood AM, Yacoub JH, Shea SM. Reduction of MRI signal distortion from titanium intracavitary brachytherapy applicator by optimizing pulse sequence parameters. *Brachytherapy*. 2018;17(2):377–382.
- Han S, Yin FF, Cai J. Evaluation of dosimetric uncertainty caused by MR geometric distortion in MRI-based liver SBRT treatment planning. *J Appl Clin Med Phys*. 2019;20(2):43–50.
- Stnescu T, Jaffray D. Investigation of the 4D composite MR image distortion field associated with tumor motion for MR-guided radiotherapy. *Med Phys*. 2016;43(3):1550–62.
- Martin GV, Kudchadker RJ, Bruno TL, Frank SJ, Wang J. Comparison of prostate distortion by inflatable and rigid endorectal MRI coils in permanent prostate brachytherapy imaging. *Brachytherapy*. 2018;17(2):298–305.
- Pappas EP, Seimenis I, Dellios D, Kollias G, Lampropoulos KI, Karaikos P. Assessment of sequence dependent geometric distortion in contrast-enhanced MR images employed in stereotactic radiosurgery treatment planning. *Phys Med Biol*. 2018;63(13):135006.
- Walker A, Metcalfe P, Liney G, Batumalai V, Dundas K, Glide-Hurst C, et al. MRI geometric distortion: Impact on tangential whole-breast IMRT. *J Appl Clin Med Phys*. 2016;17(5):7–19.
- Jackson AS, Reinsberg SA, Sohaib SA, Charles-Edwards EM, Mangar SA, South CP, et al. Distortion-corrected T2 weighted MRI: a novel approach to prostate radiotherapy planning. *Br J Radiol*. 2007;80(959):926–933.
- Stnescu T, Jans HS, Wachowicz K, Fallone BG. Investigation of a 3D system distortion correction method for MR images. *J Appl Clin Med Phys*. 2010;11(1):2961.



Lumeng Cui, Ph.D.



Gerald Moran, Ph.D.



Niranjana Venugopal, PhD, MSc

Contact

Niranjana Venugopal, PhD, MSc, MCCPM
Medical Physicist, Department of
Radiotherapy Physics
Assistant Professor, Department of
Radiology, University of Manitoba
CancerCare Manitoba
675 McDermott Avenue
Winnipeg, R3E 0V9
Canada
Tel.: +1 204-787-1737
nvenugopal@cancercare.mb.ca

Meet Siemens Healthineers

Varian is part of Siemens Healthineers. Together, we are ideally positioned to push the boundaries of innovation and shape the future of healthcare and cancer care. The team at Varian, a Siemens Healthineers Company, are committed to their work and are passionate about the opportunities ahead for accelerating our global patient impact and transforming oncology. In this section, we introduce you to colleagues from all over the world – people who put their heart and soul into everything they do.

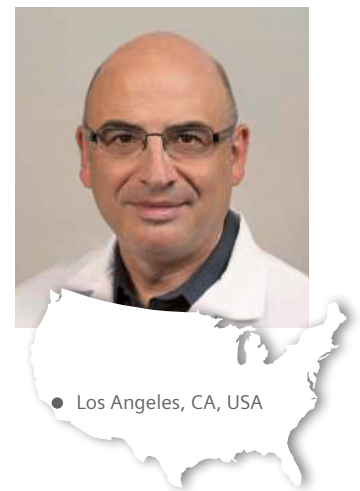
Patrick Kupelian, M.D., FASTRO

Patrick (Pat) Kupelian, M.D., is a Professor of Radiation Oncology at UCLA. He is VP of Medical Affairs at Varian Medical Systems.

Pat graduated with a BS in biology from the American University of Beirut, Lebanon, in 1985. Four years later, he earned his medical degree from the same institution. After an internship at the American University of Beirut Medical Center, Pat completed his residency in radiation oncology at the University of Texas M.D. Anderson Cancer Center in Houston, TX, USA, and completed a fellowship at the Cleveland Clinic Foundation. Following his fellowship, he was the section head of genitourinary malignancies in the Department of Radiation Oncology at the Cleveland Clinic for 8 years. He also served as the Clinical Research Director of the Department of Radiation Oncology at the Cleveland Clinic Foundation.

He is affiliated with several hospitals in the Los Angeles area, including Ronald Reagan UCLA Medical Center and UCLA Santa Monica Medical Center. Although he specializes in genitourinary malignancies, he is an internationally known expert in the development and evaluation of cutting-edge technologies in Radiation Oncology for a variety of anatomic sites. He has pioneered high-dose hypofractionated radiation therapy for prostate cancers. He has also played a significant role in the introduction and implementation of multiple image guidance techniques in radiotherapy. He has authored more than 200 research papers, multiple review papers and book chapters.

Pat is board certified in Radiation Oncology. He is a member of the American Society of Therapeutic Radiation and Oncology (ASTRO), the European Society of Therapeutic Radiology and Oncology, American Society of Clinical Oncology, the American Urological Association and the American Brachytherapy society. He has conducted multiple educational courses at ASTRO and RSNA among others. He also serves as an examiner at the American Board of Radiology.



How did you first come into contact with MRI?

My first experiences with MRI were in the 1980s, during my medical studies in Beirut.

What do you find most motivating about your job – and what are the biggest challenges?

I'm really motivated by the fact my work has such a broad clinical impact on patient care. As for the biggest challenges, I'd have to say compliance restrictions.

What do you think are the most important developments in radiation oncology?

The most important developments we've seen recently are definitely adaptive radiotherapy and the potential to incorporate multimodality imaging information into radiotherapy delivery.

If you could do whatever you wanted for a month, what would you do?

That's easy: I'm a big fan of playing and listening to music, so I'd just spend the whole month doing that.

The entire editorial staff at University of Michigan and at Siemens Healthineers extends their appreciation to all the radiation oncologists, radiologists, technologists, physicists, experts, and scholars who donate their time and energy – without payment – in order to share their expertise with the readers of MAGNETOM Flash and the MReadings.

MAGNETOM Flash – Imprint

© 2023 by Siemens Healthcare GmbH,
All Rights Reserved

Publisher:

Siemens Healthcare GmbH
Magnetic Resonance,
Karl-Schall-Str. 6, D-91052 Erlangen, Germany

Editor-in-chief:

Antje Hellwich
(antje.hellwich@siemens-healthineers.com)

Guest editor:

Professor Yue Cao, Ph.D., FAAPM
Departments of Radiation Oncology, Radiology
and Biomedical Engineering
University of Michigan, Ann Arbor, MI, USA

Editorial Board:

Rebecca Ramb, Ph.D.; Kathrin El Nemer, M.D.;
Wellesley Were; Jane Kilkenny; Heiko Meyer, Ph.D.

Review Board:

Arun Antony Joseph, Ph.D.; Martin Requardt, Ph.D.;
Elena Nioutsikou, Ph.D.; Daniel Fischer

Copy Editing:

Sheila Regan, Jen Metcalf, UNIWORKS,
www.uni-works.org
(with special thanks to Kylie Martin)

Layout:

Agentur Baumgärtner,
Friedrichstr. 4, D-90762 Fürth, Germany

PrePress and Image Editing, Production:

Clemens Ulrich, Paul Linssen,
Siemens Healthcare GmbH

Note in accordance with § 33 Para.1 of the German Federal Data Protection Law: Despatch is made using an address file which is maintained with the aid of an automated data processing system.

MAGNETOM Flash is sent free of charge to Siemens Healthineers MR customers, qualified physicians, technologists, physicists and radiology departments throughout the world. It includes reports in the English language on magnetic resonance: diagnostic and therapeutic methods and their application as well as results and experience gained with corresponding systems and solutions. It introduces from case to case new principles and procedures and discusses their clinical potential. The statements and views of the authors in the individual contributions do not necessarily reflect the opinion of the publisher.

The information presented in these articles and case reports is for illustration only and is not intended to be relied upon by the reader for instruction as to the practice of medicine. Any health care practitioner reading this information is reminded that they must use their own learning, training and expertise in dealing with their individual patients. This material does not substitute for that duty and is not intended by Siemens Healthcare to be used for any purpose in that regard. The drugs and doses mentioned herein are consistent with the approval labeling for uses and/or indications of the drug. The treating physician bears the sole responsibility for the diagnosis and treatment of patients, including drugs and doses prescribed in connection with such use. The Operating Instructions must always be strictly followed when operating the MR system. The sources for the technical data are the corresponding data sheets. Results may vary.

Partial reproduction in printed form of individual contributions is permitted, provided the customary bibliographical data such as author's name and title of the contribution as well as year, issue number and pages of MAGNETOM Flash are named, but the editors request that two copies be sent to them. The written consent of the authors and publisher is required for the complete reprinting of an article.

We welcome your questions and comments about the editorial content of MAGNETOM Flash. Please contact us at
magnetomworld.team@siemens-healthineers.com

Manuscripts as well as suggestions, proposals and information are always welcome; they are carefully examined and submitted to the editorial board for attention. MAGNETOM Flash is not responsible for loss, damage, or any other injury to unsolicited manuscripts or other materials. We reserve the right to edit for clarity, accuracy, and space. Include your name, address, and phone number and send to the editors, address above.

MReadings: MR in RT is also available online:

www.siemens-healthineers.com/magnetom-world-rt

Not for distribution in the US

On account of certain regional limitations of sales rights and service availability, we cannot guarantee that all products included in this brochure are available through the Siemens Healthineers sales organization worldwide. Availability and packaging may vary by country and is subject to change without prior notice. Some/All of the features and products described herein may not be available in the United States.

The information in this document contains general technical descriptions of specifications and options as well as standard and optional features which do not always have to be present in individual cases, and which may not be commercially available in all countries.

Due to regulatory reasons their future availability cannot be guaranteed. Please contact your local Siemens Healthineers organization for further details.

Siemens Healthineers reserves the right to modify the design, packaging, specifications, and options described herein without prior notice. Please contact your local Siemens Healthineers sales representative for the most current information.

Note: Any technical data contained in this document may vary within defined tolerances. Original images always lose a certain amount of detail when reproduced.

Siemens Healthineers Headquarters

Siemens Healthcare GmbH
Henkestr. 127
91052 Erlangen, Germany
Phone: +49 9131 84-0
[siemens-healthineers.com](https://www.siemens-healthineers.com)

Published by Siemens Healthcare GmbH · Order No. A91MR-1100-115C-7600 · ©Siemens Healthcare GmbH, 2023

[siemens-healthineers.com/magnetom-world-rt](https://www.siemens-healthineers.com/magnetom-world-rt)